

November 6, 2006

M. SCHINNERL, M. KALTENBACHER, U. LANGER, R. LERCH, J. SCHÖBERL

An Efficient Method for the Numerical Simulation of Magneto-Mechanical Sensors and Actuators

The dynamic behavior of magneto-mechanical sensors and actuators can be completely described by Maxwell's and Navier-Lamé's partial differential equations (PDEs) with appropriate coupling terms reflecting the interactions of these fields and with the corresponding initial, boundary and interface conditions. Neglecting the displacement currents, which can be done for the classes of problems considered in this paper, and introducing the vector potential for the magnetic field, we arrive at a system of degenerate parabolic PDEs for the vector potential coupled with the hyperbolic PDEs for the displacements. Usually the computational domain, the finite element discretization, the time integration, and the solver are different for the magnetic and mechanical parts. For instance, the vector potential is approximated by edge elements whereas the finite element discretization of the displacements is based on nodal elements on different meshes. The most time consuming modules in the solution procedure are the solvers for both, the magnetical and the mechanical finite element equations arising at each step of the time integration procedure. We use geometrical multigrid solvers which are different for both parts. These multigrid solvers enable us to solve quite efficiently not only academic test problems, but also transient 3D technical magneto-mechanical systems of high complexity such as solenoid valves and electro-magnetic-acoustic transducers. The results of the computer simulation are in very good agreement with the experimental data.

1 Introduction

Magneto-mechanical sensors and actuators are used in various technical devices. For instance as force-sensors and valve-actuators in automatization-engineering, in injection-valves for diesel engines or as actuators in loudspeakers. The numerical simulation is an important tool for designing and optimizing these sensors and actuators.

The basis for the numerical simulation is a mathematical model that describes the dynamic behavior of magneto-mechanical sensors and actuators. Such kind of magneto-mechanical systems can be modeled by Maxwell's and Navier-Lamé's partial differential equations (PDEs) describing the electromagnetic field and the mechanical field, respectively. The interaction of these fields is taken into account by additional terms in the PDE systems. The mathematical model is completed by appropriate initial, boundary and interface conditions. Neglecting the displacement currents, which can be done for a wide range of sensor and actuators, and introducing the vector potential for the magnetic field, we arrive at a system of degenerate parabolic PDEs for the vector potential coupled with the hyperbolic PDEs for the displacements.

The line variational formulations (called sometimes also weak formulations) of the PDE systems are the starting point for the finite element discretization. The mechanical displacements, which are living in H^1 , are approximated by nodal tetrahedral finite elements, whereas the vector potential, which is living in $H(\text{curl})$, is discretized by edge tetrahedral finite elements. We notice that the edge finite element discretization ensures the continuity of the tangential component of vector potential. We use different meshes for approximating the mechanical displacements and the magnetic vector potential. These meshes are obtained from different refinement strategies of a common coarse mesh that represents the geometry. Special transfer operators manage the transfer of magnetic quantities from the magnetic grids to the mechanical grids and vice versa. These transfers are needed in the coupling terms.

This finite element discretization results in a large-scale second-order ordinary differential equation (ODE) system for the nodal values of the displacements that is strongly coupled with a large-scale first-order ODE system for the edge degrees of freedoms (dofs) determining the finite element approximation to the magnetic vector potential. The second-order ODE system is numerically integrated by a Newmark scheme, whereas the first-order ODE system is solved by generalized trapezoidal rule. The time integration is connected with some coupling iteration taking into account the coupling of the ODE systems in a weak way. Since the time integration schemes are implicit, we have to solve a large-scale linear mechanical system and a large-scale non-linear magnetic system at each step. The non-linearity in the magnetic system is due to the dependence of the permeability on the induction in ferromagnetic

materials. The non-linear magnetic system is solved by a fixed point iteration combined with some line-search algorithm. Finally, in both cases the arising linear systems are solved by special designed multigrid methods. The multigrid method for the mechanical system uses a block Gauss-Seidel smoother that takes into account the strong coupling of nodal displacements belonging to one node, whereas the multigrid method for the magnetic systems uses the special block smoothers proposed in [1]. An alternative multigrid technique for Maxwell's equations was proposed in [14]. The solution of these linear systems of finite element equations is certainly the most time-consuming part of the whole numerical algorithms. Thanks to the efficiency of these multigrid methods we can successfully solve not only academic test problems, but also transient 3D technical magneto-mechanical systems of high complexity such as magnetic valves and electro-magnetic-acoustic transducers.

To the best knowledge of the authors, there is neither a complete mathematical analysis of the coupled magneto-mechanical model discussed in this paper nor a complete numerical analysis of the complicated numerical algorithm presented in this paper. Therefore, in order to verify the mathematical model and the accuracy of the numerical algorithm proposed, we perform a lot of numerical simulations for real-life problem containing all difficulties which are characteristic for industrial applications and compare the numerical results with the measurements made along with the numerical simulations. The first test example is a *solenoid valve*. We create a finite element model for the computer simulation and, at the same time, we build the same solenoid valve for real experiments and measurements. Due to the construction of the valve, a full 3-D simulation of the model must be performed. Additionally, the used material is strongly nonlinear and the movement of the armature causes a displacement of the FE-mesh. Also the very low penetration-depth of the magnetic-field is a challenge for the numerical simulation.

An *electro-magnetic-acoustic transducer* (EMAT) serves as a second example. The EMAT can be considered as a 3D linear problem, because the used materials are linear and the mechanical displacements are small. Nevertheless, the dimensions of the EMAT, which are very large in comparison to the small penetration depth of the magnetic field, cause a very high number of 3D finite elements. Therefore, only 2-D simulations of EMATs were performed in the past [26].

The remaining part of the paper is organized as follows. In Section 2, we present the PDEs describing the transient behavior of the mechanical and magnetical fields, together with the appropriate initial, boundary, and interface conditions. Special emphasis is given to the discussion of the influence of the coupling terms. Section 3 introduces the variational line formulations of both field problems which are the starting point for the finite element semidiscretization. The time integration, the iterative coupling, and the multigrid handling are discussed in Section 4. The coupling of the magnetic system to an electrical network with a given voltage and its handling in our numerical scheme is also discussed in Sections 3 and 4, respectively. Section 5 deals with the computer simulation of two real-life applications and their verification by experimental results. Finally, in the last section, we give some concluding remarks.

2 Partial Differential Equations for the Magnetic and the Mechanical Fields

In this section, we briefly present the Navier-Lamé and the Maxwell PDE systems describing the dynamic mechanical behavior and the transient electromagnetic behavior of magneto-mechanical sensors and actuators, respectively. The eddy current approximation to Maxwell's equations is appropriate for our class of problems. We put special emphasis on the terms modeling the coupling of mechanical and magnetical fields. The describing equations are completed by appropriate initial, boundary and, interface conditions.

2.1 The Mechanical System

If geometrically linear elasticity and isotropic linear material are assumed, the dynamical behavior of mechanical systems can be modeled by the Navier-Lamé PDE system

$$\rho \frac{\partial^2 \vec{d}}{\partial t^2} + c \frac{\partial \vec{d}}{\partial t} - \frac{E}{2(1+\nu)} \left((\nabla \cdot \nabla) \vec{d} + \frac{1}{1-2\nu} \nabla (\nabla \cdot \vec{d}) \right) = \vec{f}_V, \quad (1)$$

where \vec{f}_V denotes the volume forces, E Young's modulus, ν the Poisson ratio, ρ the specific density and c a viscous damping of the material. On the boundary Γ_{mech} of the mechanical computational domain Ω_{mech} either the mechanical displacements \vec{d} (Dirichlet boundary) or the mechanical normal stresses $\vec{\sigma}_n$ (Neumann boundary) or a mechanical impedance are given [38]. On interfaces, the continuity of the displacements and the normal stresses is required. The initial conditions prescribed for the displacements \vec{d} and the velocities $\partial\vec{d}/\partial t$ complete the mechanical equations.

2.2 The Magnetic System and the Coupling Terms

The transient electromagnetic behavior of magneto-mechanical sensors and actuators is described by Maxwell's equations, see e.g. [37]. Neglecting high frequency displacement currents, that can be always done without restrictions for the considered class of problems, we can rewrite Maxwell's equations in the form

$$\nabla \times \vec{H} = \vec{J} \quad (\text{Ampère's law}), \quad (2)$$

$$\nabla \times \vec{E}_s = -\frac{\partial \vec{B}}{\partial t} \quad (\text{Faraday's law}), \quad (3)$$

$$\nabla \cdot \vec{B} = 0. \quad (4)$$

In equations (2) - (4) \vec{H} denotes the magnetic field strength, \vec{J} the electric current density, \vec{B} the magnetic induction and \vec{E}_s the solenoidal part of the electric field \vec{E} , which computes as

$$\vec{E} = \vec{E}_e + \vec{E}_s \quad (5)$$

with \vec{E}_e the irrotational part of \vec{E} . These equations must be completed by the constitutive relations

$$\vec{B} = \mu \vec{H}, \quad (6)$$

$$\vec{J} = \vec{J}_e + \gamma (\vec{E}_s + \vec{v} \times \vec{B}), \quad (7)$$

where \vec{v} is the velocity, γ the specific electrical conductivity and μ the permeability of the material. $\vec{J}_e = \gamma \vec{E}_e$ denotes a given current density. We mention that in ferromagnetic materials the permeability depends on the magnetic induction.

The physical quantities \vec{H} , \vec{B} and \vec{J} have to fulfill not only equations (2) - (7) but also certain interface- and boundary-conditions. In Fig.1 an eddy-current problem is shown. The regions Ω_1 and Ω_2 consist of materials with

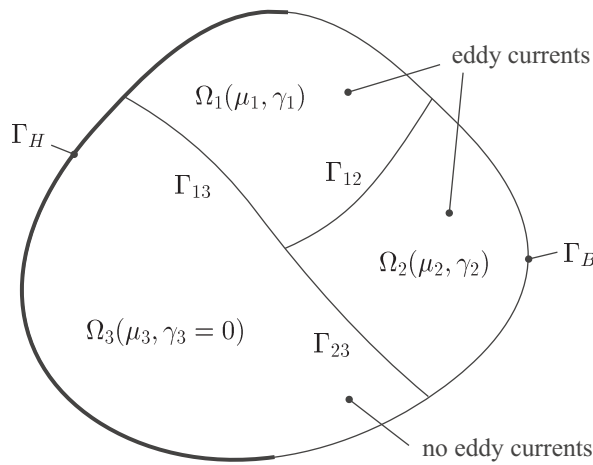


Figure 1: Model of an eddy-current problem.

the conductivities γ_1 and γ_2 . In Ω_1 and Ω_2 eddy currents can arise. The region Ω_3 has no conductivity but possibly

an impressed current \vec{J}_e . The boundary $\Gamma = \partial\Omega$ of the whole domain $\overline{\Omega} = \overline{\Omega}_1 \cup \overline{\Omega}_2 \cup \overline{\Omega}_3$ usually consists of the parts Γ_H and Γ_B with the boundary conditions

$$\vec{B} \cdot \vec{n} = 0 \quad \text{on } \Gamma_B \quad (8)$$

and

$$\vec{H} \times \vec{n} = \vec{K} \quad \text{on } \Gamma_H. \quad (9)$$

In equations (8) and (9) \vec{n} denotes the outer normal unit-vector to the boundary Γ . \vec{K} is a given surface current-density. On the interface Γ_{12} between Ω_1 and Ω_2 the interface conditions

$$\left. \begin{aligned} \vec{B}_1 \cdot \vec{n}_1 + \vec{B}_2 \cdot \vec{n}_2 &= 0, \\ \vec{H}_1 \times \vec{n}_1 + \vec{H}_2 \times \vec{n}_2 &= 0 \end{aligned} \right\} \quad \text{on } \Gamma_{12} \quad (10)$$

$$(11)$$

must hold. The normal unit-vectors are oriented in opposite direction which means that

$$\vec{n}_2 = -\vec{n}_1. \quad (12)$$

Furthermore, since the current \vec{J} is divergence-free, the condition

$$\vec{J}_1 \cdot \vec{n}_1 + \vec{J}_2 \cdot \vec{n}_2 = 0 \quad (13)$$

must hold on Γ_{12} , too. On the boundaries Γ_{13} and Γ_{23} , analogous conditions must be valid.

Introducing a magnetic vector potential \vec{A}

$$\vec{B} = \nabla \times \vec{A} \quad (14)$$

leads according to equation (3) to the relation

$$\vec{E}_s = -\frac{\partial \vec{A}}{\partial t}, \quad (15)$$

so that we can transfer equations (2)-(7) to the form

$$\gamma \frac{\partial \vec{A}}{\partial t} + \nabla \times \left(\frac{1}{\mu} \nabla \times \vec{A} \right) + -\gamma \vec{v} \times (\nabla \times \vec{A}) = \vec{J}_e. \quad (16)$$

For large Péclet-numbers

$$Pe = \frac{\mu \gamma v h}{2} \gg 1, \quad (17)$$

the term $\gamma \vec{v} \times (\nabla \times \vec{A})$ becomes dominant and causes instabilities in the numerical solution process [24]. In (17), h denotes the discretization parameter in direction of the velocity \vec{v} . However, if due to mechanical movements / deformations the overall magnetic field is changed (e.g., movement of the armature in a magnetic valve), we have to consider the formulation of the magnetic problem on the deformed geometry [24]. Observing some point P in a fixed reference frame $\Gamma(x, y, z)$ (see Fig. 2), we can express the spatial and temporal variation of the magnetic vector potential \vec{A} at this point by the formula

$$\begin{aligned} \frac{\Delta \vec{A}}{\Delta t} &= \frac{\vec{A}(\vec{d} + \Delta \vec{d}, t + \Delta t) - \vec{A}(\vec{d}, t)}{\Delta t} \\ &= \frac{\vec{A}(\vec{d} + \Delta \vec{d}, t + \Delta t) - \vec{A}(\vec{d}, t + \Delta t)}{\Delta t} + \frac{\vec{A}(\vec{d}, t + \Delta t) - \vec{A}(\vec{d}, t)}{\Delta t}. \end{aligned}$$

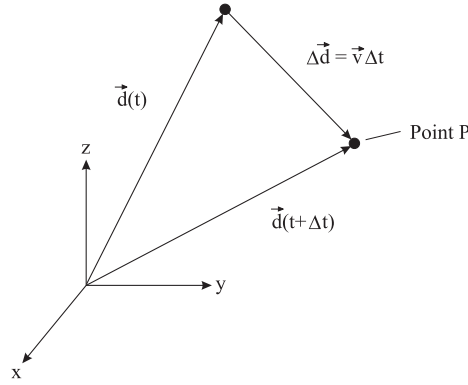


Figure 2: Movement of a considered point P.

For $\Delta t \rightarrow 0$, the expression (18) leads to the relation

$$\frac{d\vec{A}}{dt} = \frac{\partial \vec{A}}{\partial t} + (\vec{v} \cdot \nabla) \vec{A}. \quad (18)$$

On the other hand, the electromotive force can be rewritten as¹

$$\vec{v} \times (\nabla \times \vec{A}) = \nabla_{\vec{A}}(\vec{v} \cdot \vec{A}) - (\vec{v} \cdot \nabla) \vec{A}. \quad (19)$$

Using (18) and (19), we can transform the partial differential equation (16) into the form

$$\gamma \frac{d\vec{A}}{dt} + \nabla \times \left(\frac{1}{\mu} \nabla \times \vec{A} \right) - \gamma \nabla_{\vec{A}}(\vec{v} \cdot \vec{A}) = \vec{J}_e. \quad (20)$$

Equation (20) illustrates, that the total differential $d\vec{A}/dt$ takes the induced current caused by the electromotive force implicitly into account, but in return the term $\gamma \nabla_{\vec{A}}(\vec{v} \cdot \vec{A})$ must be considered additionally. If \vec{v} and \vec{A} are orthogonal, this term disappears, which is the case for all 2D problems. Besides the electromotive force, also magnetic forces cause a coupling between the magnetic and the mechanical field. The magnetic volume-force, produced by the magnetic field, can be separated into two parts. The first effect is the Lorentz-force,

$$\vec{f}_{V,L} = \vec{J} \times \vec{B}, \quad (21)$$

which occurs when a magnetic induction \vec{B} exists in a body with a current-density \vec{J} . Using the magnetic vector potential \vec{A} , (21) can be rewritten as

$$\vec{f}_{V,L} = \left(\vec{J}_e - \gamma \frac{d\vec{A}}{dt} + \gamma \nabla_{\vec{A}}(\vec{v} \cdot \vec{A}) \right) \times (\nabla \times \vec{A}). \quad (22)$$

In the case of non-constant permeability, especially in the presence of ferromagnetic materials, an additional force

$$\vec{f}_{V,\mu} = -\frac{1}{2} \left| \frac{1}{\mu} \nabla \times \vec{A} \right|^2 \nabla \mu \quad (23)$$

arises. At an interface between two materials with the permeabilities μ_1 and μ_2 , the volume-force formulation (23) can be transferred into Maxwell's surface force-density formulation [37]

$$\vec{f}_\Gamma = (\vec{n} \cdot \vec{H}) \vec{B} - \vec{n} \frac{1}{2} \vec{B} \cdot \vec{H}. \quad (24)$$

¹ $\nabla_{\vec{A}}(\vec{v} \cdot \vec{A})$ means, that the gradient is used only for the terms of the magnetic vector potential \vec{A} .

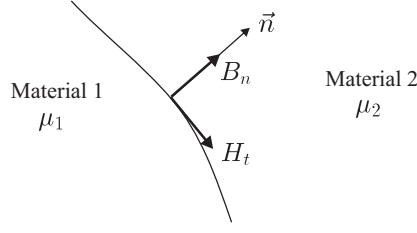


Figure 3: Interface between two materials with different permeabilities.

This formulation can also be written with the help of a tensor $[T]$, which allows the calculation of the magnetic force and moment acting to a body by the equations (see [36], pp. 154–155, and [18])

$$\vec{F} = \oint_{\vec{A}} [T] d\vec{A} \quad (25)$$

and

$$\vec{M} = \oint_{\vec{A}} \vec{r} \times ([T] d\vec{A}). \quad (26)$$

We mention that (24) must not consider the jump of the magnetic permeability at the interface of the ferromagnetic material. So it is sufficient to calculate (24) only at the finite elements of the non-ferromagnetic domain which are connected to the interface.

For problems with permanent-magnetic materials the additional force term

$$\vec{f}_{V3} = -\vec{H} \nabla \cdot \vec{M} \quad (27)$$

must be considered. \vec{M} is the magnetization of the used permanent magnetic material. At last the magnetostriction coupling effect is described by

$$\vec{f}_{V4} = \int_0^H \nabla \left(|\vec{H}|^2 \rho \frac{\partial \mu}{\partial \rho} \right) d\vec{H}, \quad (28)$$

where ρ denotes the specific density. Magnetostrictive actuators are especially suited for the generation of high forces. But this effect is not covered here.

3 Variational Formulation and Finite Element Discretization

This section provides the variational formulations of the mechanical and magnetic PDE systems which are, of course, coupled. The coupled variational formulations are the starting point for the finite element semi-discretization that results into a second-order mechanical ODE system and a first-order magnetic ODE system which are again coupled. Finally, we describe a magnetic system that is coupled to an electrical network with an impressed voltage.

3.1 Mechanical System

By multiplying the mechanical differential equation (1) with a weighting function \vec{w} and integrating over the domain Ω_{mech} , the mechanical problem is transferred to the weak form

$$\int_{\Omega} \left(\rho \frac{\partial^2 \vec{d}}{\partial t^2} + c \frac{\partial \vec{d}}{\partial t} - \frac{E}{2(1+\nu)} \left((\nabla \cdot \nabla) \vec{d} + \frac{1}{1-2\nu} \nabla(\nabla \cdot \vec{d}) \right) \right) \cdot \vec{w} d\Omega = \int_{\Omega} \vec{f}_V \cdot \vec{w} d\Omega. \quad (29)$$

Using Green's first identity and the symmetry of the stress tensor, we obtain the variational formulation or the so-called weak form [16]

$$\int_{\Omega_{mech}} \rho \frac{\partial^2 d_i}{\partial t^2} w_i d\Omega + \int_{\Omega_{mech}} \vec{\epsilon}(\vec{d})^T \mathbf{D} \vec{\epsilon}(\vec{w}) d\Omega + \int_{\Omega_{mech}} c \frac{\partial d_i}{\partial t} w_i d\Omega = \int_{\Omega_{mech}} f_i w_i d\Omega + \int_{\Gamma_{ni}} \sigma_{ni} w_i d\Gamma \quad (30)$$

of (1), see e.g. [16]. In (30), i denotes the spatial direction (x, y or z), $\vec{\epsilon}$ the components of the mechanical strain tensor in Voigt notation, \mathbf{D} the tensor of the elastic coefficients, and Γ_{ni} the boundary with given surface stress σ_{ni} . The mechanical domain is now discretized with the help of nodal finite elements. Thereby, the mechanical displacements are approximated in the form

$$\vec{d} \approx \sum_{k=1}^{n_n} N_k \vec{d}_k, \quad (31)$$

where N_k denotes the shape function of the k -th node, \vec{d}_k the displacement at the k -th node and n_n the number of nodes. By using (31) in (30) and applying Galerkin's technique, the system of second-order ordinary differential equations (ODE)

$$\mathbf{M} \left\{ \frac{\partial^2 d}{\partial t^2} \right\} + \mathbf{C} \left\{ \frac{\partial d}{\partial t} \right\} + \mathbf{K} \{d\} = \{F\} \quad (32)$$

is obtained, where the mass matrix \mathbf{M} , the stiffness matrix \mathbf{K} and the force vector $\{F\}$ have the following form:

- mass matrix:

$$\begin{aligned} \mathbf{M} &= [M_{ab}] \\ M_{ab} &= \delta_{ij} \int_{\Omega} N_a \rho N_b d\Omega \\ 1 \leq a, b &\leq n_{eq} \\ 1 \leq i, j &\leq n_{sd} \end{aligned} \quad (33)$$

- stiffness matrix:

$$\begin{aligned} \mathbf{K} &= [K_{ab}] \\ K_{ab} &= \vec{e}_i^T \int_{\Omega} \mathbf{B}_a^T \mathbf{D} \mathbf{B}_b d\Omega \vec{e}_j \\ 1 \leq a, b &\leq n_{eq} \\ 1 \leq i, j &\leq n_{sd} \end{aligned} \quad (34)$$

in the 3D case:

$$\mathbf{B}_a = \begin{pmatrix} \frac{\partial N_a}{\partial x} & 0 & 0 \\ 0 & \frac{\partial N_a}{\partial y} & 0 \\ 0 & 0 & \frac{\partial N_a}{\partial z} \\ 0 & \frac{\partial N_a}{\partial z} & \frac{\partial N_a}{\partial y} \\ \frac{\partial N_a}{\partial z} & 0 & \frac{\partial N_a}{\partial x} \\ \frac{\partial N_a}{\partial y} & \frac{\partial N_a}{\partial x} & 0 \end{pmatrix} \quad (35)$$

• force vector:

$$\begin{aligned} \{F\} &= \{F_a\} \\ F_a &= \int_{\Omega} N_a f_i d\Omega + \int_{\Gamma_{ni}} N_a \sigma_{ni} d\Gamma \end{aligned} \quad (36)$$

In (33) - (36) n_{eq} denotes the number of unknowns, \vec{e}_i the unity vector in the spatial direction i , δ_{ij} Kronecker's operator and n_{sd} the spatial dimension of the mechanical field. The damping matrix \mathbf{C} is chosen as a linear combination of \mathbf{M} and \mathbf{K} [5], i.e.

$$\mathbf{C} = \alpha \mathbf{M} + \beta \mathbf{K}. \quad (37)$$

The magnitudes of the Rayleigh coefficients α and β depend on the energy dissipation characteristics of the modeled mechanical problem.

3.2 Magnetic System

By multiplying the magnetic system (20) with a weighting function \vec{W} , integrating over the domain $\Omega_{mag}(\vec{d})$, which is deformed by the mechanical displacement \vec{d} , and applying the first Green's identity, the magnetic field can be expressed in a weak sense by the variational formulation

$$\begin{aligned} \int_{\Omega_{mag}} \gamma \frac{d\vec{A}}{dt} \cdot \vec{W} d\Omega + \int_{\Omega_{mag}} \frac{1}{\mu} (\nabla \times \vec{A}) \cdot (\nabla \times \vec{W}) d\Omega - \int_{\Omega_{mag}} \gamma \nabla_{\vec{A}}(\vec{v} \cdot \vec{A}) \cdot \vec{W} d\Omega = \\ \int_{\Omega_{mag}} \vec{J}_e \cdot \vec{W} d\Omega + \int_{\Gamma_{mag,H}} (\vec{H} \times \vec{n}) \cdot \vec{W} d\Gamma, \end{aligned} \quad (38)$$

where $\Gamma_{mag,H}$ denotes a boundary with specified $\vec{H} \times \vec{n}$. In order to achieve an appropriate FE-discretization of

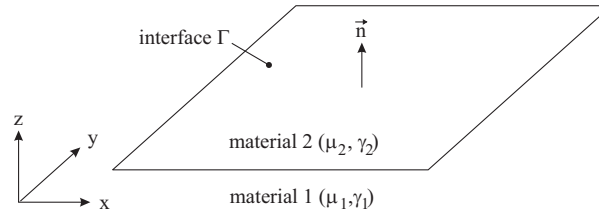


Figure 4: Interface between two materials.

the magnetic system, the properties of the magnetic field at an interface must be analyzed in a more detailed way. In Fig. 4 an interface between two materials with the permeabilities μ_1 and μ_2 and the conductivities γ_1 and γ_2 is

displayed. For simplicity and without loss of generality, the interface lies in the x-y plane and the normal-vector \vec{n} is exactly oriented in z-direction. Using (14) and (10), the condition

$$B_n = B_z = \frac{\partial A_{y1}}{\partial x} - \frac{\partial A_{x1}}{\partial y} = \frac{\partial A_{y2}}{\partial x} - \frac{\partial A_{x2}}{\partial y} \quad (39)$$

must be fulfilled. Equation (39) can be enforced explicitly, if the tangential component of \vec{A} is continuous at the interface. As mentioned in sect. 2.2 displacement currents are neglected, which enables the reformulation of (13) on an interface between two eddy-current regions as

$$\vec{n} \cdot \gamma_1 \frac{\partial \vec{A}_1}{\partial t} = \vec{n} \cdot \gamma_2 \frac{\partial \vec{A}_2}{\partial t}. \quad (40)$$

Therefore, in z direction, equation

$$\frac{\partial}{\partial t} [\gamma_1 A_{z1} - \gamma_2 A_{z2}] = 0 \quad (41)$$

must hold. As the magnetic vector potential is not static, (41) requires discontinuity of A_z if $\gamma_1 \neq \gamma_2$. For nodal finite elements one needs a splitting of the magnetic vector potential in a new vector, which has to be divergence free, and a gradient of a scalar potential (corresponds to a decomposition of the space $H(\text{curl})$). In addition, a weighted regularization according to [7] has to be applied. For a detailed discussion we refer to [19]. The “natural” choice of the spatial discretization are edge-finite-elements [28]. Thereby, the degrees of freedom are not attached to the element nodes, but to the element edges. In Fig. 5 a linear edge-tetrahedron-element is shown. Using the edge

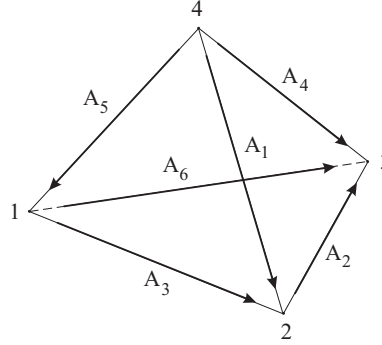


Figure 5: Linear edge tetrahedron.

element discretization, the magnetic vector field \vec{A} is approximated by

$$\vec{A} \approx \sum_{k=1}^{n_k} \vec{N}_k A_k. \quad (42)$$

In (42), \vec{N}_k denotes the vectorial shape function, which is associated with the k-th edge e_k , n_k the number of edges in the magnetic FE mesh, and

$$A_k = \int_{e_k} \vec{A} \cdot d\vec{s} \quad (43)$$

approximates the line-integral over the projection of the magnetic vector potential \vec{A} to the k-th edge e_k . Inserting (42) into the weak formulation (38) leads to the first-order ODE system

$$\mathbf{L} \left\{ \frac{dA}{dt} \right\} + \mathbf{P}\{A\} + \mathbf{P2}(\vec{v})\{A\} = \{Q\}. \quad (44)$$

The conductivity matrix \mathbf{L} , the permeability matrix \mathbf{P} , the second permeability matrix $\mathbf{P2}$ and the source vector $\{Q\}$ have the form:

- conductivity matrix:

$$\begin{aligned}
\mathbf{L} &= [L_{ab}] \\
L_{ab} &= \int_{\Omega_{mag}(\vec{d})} \vec{N}_a \cdot \gamma \vec{N}_b d\Omega \\
1 \leq a, b &\leq n_k
\end{aligned} \tag{45}$$

- permeability matrix:

$$\begin{aligned}
\mathbf{P} &= [P_{ab}] \\
P_{ab} &= \int_{\Omega_{mag}(\vec{d})} \left(\frac{1}{\mu} \nabla \times \vec{N}_a \right) \cdot (\nabla \times \vec{N}_b) d\Omega \\
1 \leq a, b &\leq n_k
\end{aligned} \tag{46}$$

- permeability matrix 2:

$$\begin{aligned}
\mathbf{P2} &= [P2_{ab}] \\
P2_{ab} &= - \int_{\Omega_{mag}(\vec{d})} \gamma \nabla_{\vec{A}} (\vec{v} \cdot \vec{N}_a) \cdot \vec{N}_b d\Omega \\
1 \leq a, b &\leq n_k
\end{aligned} \tag{47}$$

- source vector:

$$\begin{aligned}
\{Q\} &= \{Q_b\} \\
Q_b &= \int_{\Omega_{mag}(\vec{d})} \vec{N}_a \cdot \vec{J}_e d\Omega \\
1 \leq b &\leq n_k
\end{aligned} \tag{48}$$

Here, the boundary integral term in (38) is assumed to be zero.

The solution of (44) requires special care in order to obtain an optimal solver. We suggest to add a fictive electric conductivity γ' to regions with zero electric conductivity to obtain a variational form, which is H(curl)-elliptic. Of course, this fictive conductivity γ' has to be chosen small as compared to the reluctivity of the material. The proof of convergence even in the case of $\gamma' \rightarrow 0$ is given in [30] and [3] for the magnetostatic case and for the eddy current case, respectively.

3.3 Voltage Loading

Frequently the magnetic system (20) is not excited by a given current density \vec{J}_e , but is coupled to an electrical network with a given voltage U . In Fig. 6, the simplest case of an electrical network, consisting of the coil resistor R_{coil} placed in series with the FE-model is shown. Thereby, not only the magnetic vector potential \vec{A} , but also the current I is unknown. The network is described by

$$U = R_{coil} I + \frac{\partial \Psi}{\partial t}, \tag{49}$$

where the interlinkage flux is determined by

$$\Psi = \frac{n_c}{S_c} \int_{\Omega_j} \vec{A} \cdot \vec{n}_s d\nu. \tag{50}$$

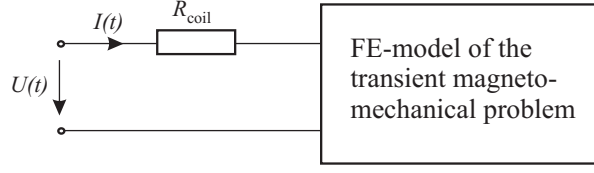


Figure 6: External electrical network.

In (50), n_c denotes the number of turns of the coil in the FE model, S_c the crosssectional area of the coil, \vec{n}_s the unit tangential vector along the direction of the exciting current and Ω_j the region of the coil. On the other hand, the current density \vec{J}_e in the coil is described by

$$\vec{J}_e = \frac{n_c}{S_c} I \vec{n}_s. \quad (51)$$

To solve the coupled magnetic system a technique presented in [33], sect. 5.3.3 is applied. Using (50) in (49) and (51) in (44), the coupled system can be written in the discrete form as

$$\mathbf{L}\left\{\frac{dA}{dt}\right\} + \mathbf{P}\{A\} + \mathbf{P2}(\vec{v})\{A\} = \mathbf{u}I, \quad (52)$$

$$R_{\text{coil}} I + \mathbf{u}^T \left\{\frac{dA}{dt}\right\} = U. \quad (53)$$

Thereby, the coupling vector \mathbf{u} has the form

$$\mathbf{u} = \frac{n_c}{S_c} \int_{\Omega_j} \vec{N}_i \cdot \vec{n}_s d\nu \in \mathbb{R}^{N_e}, \quad (54)$$

where N_e denotes the number of edges in the considered FE mesh.

4 Time Integration, Iterative Coupling and Solution

A mathematically strong coupling of the mechanical and the magnetic system in one large equation system is hard to realize, because the electromotive force is a non-linear term, i.e., both fields contribute directly to this effect. Additionally, the Lorentz force and the interface force, caused by variations of the magnetic permeability, are quadratic functions of the magnetic vector potential \vec{A} . Therefore, an iterative coupling mechanism, used for instance in [31] and [20], is applied. Therewith, it is possible to consider variations of the magnetic field, which are caused by the mechanical displacement \vec{d} , easily. In order to achieve a good adaptation of the FE meshes to the mechanical and magnetic fields, two different grids are used for both physical fields. Therefore, it is necessary to transfer data, like the mechanical displacement \vec{d} or the magnetic volume-force \vec{f}_V , between the edge element discretization of the magnetic field and the nodal element discretization of the mechanical field. The time discretization of the mechanical and the magnetic system is achieved by implicit time stepping algorithms. The large-scale systems of mechanical FE equations are solved by a geometrical multigrid method whereas the non-linear system of magnetic FE equations are solved by multigrid combined with a fixed point iteration.

4.1 Time Discretization of the Mechanical and the Magnetic Systems

The time discretization of the second-order mechanical ODE system (32) is performed by using Newmark's technique [16]. In order to shorten the notation, the velocity $\{\partial \vec{d} / \partial t\}$ and the acceleration $\{\partial^2 \vec{d} / \partial t^2\}$ at the nodes are abbreviated by $\{v\}$ and $\{a\}$, respectively. In addition to this, the curved brackets for the FE nodal and edge values

are omitted. The index n denotes the variable at the time moment $n\Delta t$, where Δt denotes the used time step. Applying Newmark's technique gives the equations

$$\mathbf{M}a_{n+1} + \mathbf{C}v_{n+1} + \mathbf{K}d_{n+1} = F_{n+1} \quad (55)$$

for defining

$$d_{n+1} = d_n + \Delta t v_n + \frac{\Delta t^2}{2}[(1 - 2\beta)a_n + 2\beta a_{n+1}], \quad (56)$$

$$v_{n+1} = v_n + \Delta t[(1 - \gamma)a_n + \gamma a_{n+1}], \quad (57)$$

where β and γ denote Newmark's parameters which control the stability and accuracy of the method.

The first-order magnetic ODE system (44) is numerically integrated by the use of the generalized trapezoidal rule giving the equations

$$\mathbf{L}R_{n+1} + \mathbf{P}A_{n+1} + \mathbf{P2}(\vec{v}_{n+1})A_{n+1} = Q_{n+1} \quad (58)$$

for defining

$$A_{n+1} = A_n + \Delta t R_{n+\alpha}, \quad (59)$$

$$R_{n+\alpha} = (1 - \alpha)R_n + \alpha R_{n+1}, \quad (60)$$

where the abbreviation R is used for the time derivation $\partial A / \partial t$ of the edge dofs [16].

4.2 Iterative Coupling of the Mechanical and Magnetic Systems

The time discretization methods of the mechanical and magnetic systems are coupled by an iterative technique handling the coupling of the mechanical and magnetic parts (k denotes the iteration counter and n the time step counter):

- **Step 1:** Calculation of a first approximation to the mechanical displacement and velocity on the mechanical mesh \mathcal{M}_{mech} :

$$d_{n+1}^k = d_n + \Delta t v_n + \frac{\Delta t^2}{2} a_n, \quad (61)$$

$$v_{n+1}^k = v_n + \Delta t a_n. \quad (62)$$

- **Step 2:** Projection of d_{n+1}^k and v_{n+1}^k from \mathcal{M}_{mech} to the magnetic mesh \mathcal{M}_{mag} .
- **Step 3:** Distortion of the magnetic mesh \mathcal{M}_{mag} by d_{n+1}^k . Reassembling of the conductivity-matrix \mathbf{L} and the permeability matrix \mathbf{P} at the deformed geometry. According to (18), the total differential of the magnetic vector potential is calculated by this updating and, thereby, the electromotive force is implicitly taken into account. Additionally, the variation of the magnetic field, caused by the mechanical displacement, is considered by the updating process.
- **Step 4:** Calculation of the magnetic system:

- The matrix $\mathbf{P2}(\vec{v})$ is non-symmetric and depends on the velocity \vec{v} , therefore, this term is only approximated by a predictor value:

$$A_{n+1}^{app} = \begin{cases} A_n + \Delta t R_n & k = 1 \\ A_{n+1}^k & \text{otherwise} \end{cases} \quad (63)$$

$$\mathbf{P2}(v_{n+1})A_{n+1} := \mathbf{P2}(v_{n+1}^k)A_{n+1}^{app}. \quad (64)$$

- Solve the system

$$\mathbf{L}^* R_{n+1}^{k+1} = Q_{n+1} - \mathbf{P} A_n - (1 - \alpha) \Delta t \mathbf{P} R_n - \mathbf{P} \mathbf{2}(v_{n+1}^k) A_{n+1}^{app}, \quad (65)$$

with the system matrix

$$\mathbf{L}^* = \mathbf{L} + \alpha \Delta t \mathbf{P}. \quad (66)$$

- Correct the vector potential:

$$A_{n+1}^{k+1} = A_n + (1 - \alpha) \Delta t R_n + \alpha \Delta t R_{n+1}^{k+1}. \quad (67)$$

- **Step 5:** Calculation of the magnetic induction \vec{B} and the magnetic forces \vec{f}_V .
- **Step 6:** Projection of \vec{f}_V to the mechanical FE mesh \mathcal{M}_{mech} .
- **Step 7:** Calculation of the mechanical field:

- Predictor:

$$\tilde{d}_{n+1} = d_n + \Delta t v_n + \frac{\Delta t^2}{2} (1 - 2\beta) a_n, \quad (68)$$

$$\tilde{v}_{n+1} = v_n + (1 - \gamma) \Delta t a_n. \quad (69)$$

- Solve the system

$$\mathbf{M}^* a_{n+1}^{k+1} = F_{n+1} - \mathbf{C} \tilde{v}_{n+1} - \mathbf{K} \tilde{d}_{n+1} \quad (70)$$

with the system matrix

$$\mathbf{M}^* = \mathbf{M} + \gamma \Delta t \mathbf{C} + \beta \Delta t^2 \mathbf{K}. \quad (71)$$

- Corrector:

$$d_{n+1}^{k+1} = \tilde{d}_{n+1} + \beta \Delta t^2 a_{n+1}^{k+1} \quad (72)$$

$$v_{n+1}^{k+1} = \tilde{v}_{n+1} + \gamma \Delta t a_{n+1}^{k+1} \quad (73)$$

- **Step 8:** Convergence test:

$$\|d_{n+1}^{k+1} - d_{n+1}^k\|_2 < \epsilon \|d_{n+1}^{k+1}\|_2 \quad (\epsilon \approx 10^{-3}) \quad (74)$$

If no convergence is reached, return to step 2.

- **Step 9:** Proceed with the next time step.

We mention that for practical problems only a very low number of iterations per time step is necessary. The time-integration parameters α , β and γ are chosen with 0.5, 0.25 and 0.5.

4.3 Calculation of the Magnetic Field in the Presence of Ferromagnetic Materials

Ferromagnetic materials have a non-constant magnetic permeability μ . Thereby, the non-linear relation

$$\vec{H} = \frac{1}{\mu(\vec{B})} \vec{B}. \quad (75)$$

holds. It is assumed, that the material is isotropic, i.e. that μ is equal in each direction, and that no hysteresis effects arise. In the nonlinear case, system (65) has the form

$$\mathbf{L}^*(A) R_{n+1} = Q_{n+1} - \mathbf{P}(A) A_n - (1 - \alpha) \Delta t \mathbf{P}(A) R_n - \mathbf{P} \mathbf{2}(v_{n+1}^{app}) A_{n+1}^{app}. \quad (76)$$

In (76), the modified conductivity matrix \mathbf{L}^* and the permeability matrix \mathbf{P} depend on the edge degrees of freedom. The nonlinear magnetic field is calculated by a fixed-point method [35], which is described by the following algorithm:

- **Step 1:** Calculation of an initial guess A_{n+1}^i by using the variables of the time step n :

$$i = 0, \quad (77)$$

$$A_{n+1}^i = A_n + \Delta t R_n, \quad (78)$$

$$R_{n+1}^i = 0. \quad (79)$$

- **Step 2:** Reassembling of the matrices \mathbf{L}^* and \mathbf{P} .
- **Step 3:** Calculation of improved guesses R_{n+1}^{i+1} and A_{n+1}^{i+1} :

$$\mathbf{L}^*(A_{n+1}^i)R_{n+1}^{i+1} = Q_{n+1} - \mathbf{P}(A_{n+1}^i)A_n - (1 - \alpha)\Delta t \mathbf{P}(A_{n+1}^i)R_n - \mathbf{P2}(v_{n+1}^A)A_{n+1}^i, \quad (80)$$

$$A_{n+1}^{i+1} = A_n + (1 - \alpha)\Delta t R_n + \alpha\Delta t R_{n+1}^{i+1}. \quad (81)$$

- **Step 4:** Convergence test:

– IF

$$\|R_{n+1}^{i+1} - R_{n+1}^i\| \geq \epsilon \|R_{n+1}^i\| \quad (82)$$

– THEN $i = i + 1$ and return to Step 2

– ELSE proceed with the next time step.

In many cases this algorithm is oscillating or only slowly convergent. However, the method can be stabilized by a line-search algorithm [35]. Thereby, **Step 3** of the iteration must be modified as follows:

- **Step 3.1:** Calculation of improved guesses R_{n+1}^i and A_{n+1}^i .
- **Step 3.2:** Calculation of a search direction

$$\delta R_{n+1} = R_{n+1}^{i+1} - R_{n+1}^i, \quad (83)$$

$$\delta A_{n+1} = A_{n+1}^{i+1} - A_{n+1}^i. \quad (84)$$

- **Step 3.3:** Choosing of a relaxation parameter τ and calculation of modified guesses

$$R_{n+1}^\tau = R_{n+1}^i + \tau \delta R_{n+1}, \quad (85)$$

$$A_{n+1}^\tau = A_{n+1}^i + \tau \delta A_{n+1}. \quad (86)$$

- **Step 3.4:** Reassembling of \mathbf{L}^* and \mathbf{P} and calculation of the residual $\Psi(\tau)$ and the projection of the residual to the search direction $G(\tau)$:

$$\Psi(\tau) = \mathbf{L}^* R_{n+1}^\tau - Q_{n+1} + \mathbf{P} A_{n+1}^\tau + \mathbf{P2}(v_{n+1}^{app}) A_{n+1}^{app}, \quad (87)$$

$$G(\tau) = \delta R_{n+1} \cdot \Psi(\tau). \quad (88)$$

Now, the relaxation parameter τ is chosen in such a way that the projection of the residual to the search direction is a minimum. Since even for strong nonlinear materials $G(\tau)$ is approximately a linear function of τ , it is sufficient to calculate $G(\tau)$ for two different values of τ and to determine the optimal τ with linear interpolation. This method leads to a fast convergent and very stable solution process with comparatively low numerical effort in the case of applying a full multigrid method.

4.4 Modifications in the Case of Voltage Loading

One possibility to take into account the external network is the coupling of (52) and (53) in one coupled system [31]. Thereby, the structure of the arising system matrix is destroyed, which may lead to a slower convergence of the used iterative MG solvers. Therefore, in this paper an alternative strong coupling method of the magnetic field and the network is chosen, which preserves the structure of the system matrix. By multiplying (52) with the inverse modified mass matrix $(\mathbf{L}^*)^{-1}$, we obtain

$$R_{n+1} = (\mathbf{L}^*)^{-1} \mathbf{u} I_{n+1} - (\mathbf{L}^*)^{-1} [\mathbf{P} A_n - (1 - \alpha) \Delta t \mathbf{P} R_n - \mathbf{P} \mathbf{2}(v_{n+1}^k) A_{n+1}^{app}]. \quad (89)$$

Using the abbreviation

$$\tilde{A}_{n+1} = \mathbf{P} A_n - (1 - \alpha) \Delta t \mathbf{P} R_n - \mathbf{P} \mathbf{2}(v_{n+1}^{app}) A_{n+1}^{app} \quad (90)$$

and inserting (89) in the time discretized form of (53), we arrive at the relation

$$U_{n+1} = \mathbf{u}^T (\mathbf{L}^*)^{-1} \mathbf{u} I_{n+1} + R_{\text{coil}} I_{n+1} - \mathbf{u}^T (\mathbf{L}^*)^{-1} \tilde{A}_{n+1}, \quad (91)$$

which can be rewritten in the form

$$I_{n+1} = \frac{U_{n+1} + \mathbf{u}^T (\mathbf{L}^*)^{-1} \tilde{A}_{n+1}}{\mathbf{u}^T (\mathbf{L}^*)^{-1} \mathbf{u} + R_{\text{coil}}}. \quad (92)$$

Therefore, in the case of voltage loading, the calculation of the magnetic field at each time step is modified as follows:

- Approximations:

$$A_{n+1}^{app} = \begin{cases} A_n + \Delta t R_n & k = 1 \\ A_{n+1}^k & \text{else} \end{cases} \quad (93)$$

$$\mathbf{P} \mathbf{2}(v_{n+1}) A_{n+1} = \mathbf{P} \mathbf{2}(v_{n+1}^k) A_{n+1}^{app}. \quad (94)$$

- Equation:

$$\tilde{A}_{n+1} = \mathbf{P} A_n - (1 - \alpha) \Delta t \mathbf{P} R_n - \mathbf{P} \mathbf{2}(v_{n+1}^k) A_{n+1}^{app}, \quad (95)$$

$$I_{n+1} = \frac{U_{n+1} + \mathbf{u}^T (\mathbf{L}^*)^{-1} \tilde{A}_{n+1}}{\mathbf{u}^T (\mathbf{L}^*)^{-1} \mathbf{u} + R_{\text{coil}}}, \quad (96)$$

$$R_{n+1} = (\mathbf{L}^*)^{-1} \mathbf{u} I_{n+1} - (\mathbf{L}^*)^{-1} \tilde{A}_{n+1}. \quad (97)$$

- Corrector:

$$A_{n+1} = A_n + (1 - \alpha) \Delta t R_n + \alpha \Delta t R_{n+1}. \quad (98)$$

The terms $(\mathbf{L}^*)^{-1} \mathbf{u}$ and $(\mathbf{L}^*)^{-1} \tilde{A}$ of (97) are already known from (96) and, it is not necessary to calculate them again. Additionally, in the linear case the term $(\mathbf{L}^*)^{-1} \mathbf{u}$ is constant and must be calculated only for the first time step. Therefore, only the equation system

$$\mathbf{L}^* \xi = \tilde{A} \quad (99)$$

has to be solved at each iteration step. We mention that in case of voltage loading and non-linear magnetic problems, the presented line-search algorithm is also applied to (96) and (97).

4.5 Multigrid Solvers for the Linear Mechanical and Magnetic Systems

In the iterative simulation technique presented above, the solution of the mechanical system (65) and the magnetic system (70) are certainly the parts with the highest computational effort. These equations are solved by multigrid methods which are known to be asymptotically optimal with respect to computational costs. In [12] an excellent introduction to these solution techniques is given. To apply multigrid solvers to (65) and (70), the special properties of the magnetic and mechanical fields and their discretizations must be taken into account. The mechanical problem is discretized by nodal elements with three degrees of freedom at each node. Since a strong coupling effect between the degrees of freedom of one node arises, a multigrid technique with block Gauss-Seidel smoothing is used [2]. The magnetic field is discretized by means of edge elements. To achieve a fast and robust multigrid solution process, for this problem a special multigrid technique with overlapping block smoothers is applied [1].

4.6 Transformation of Field Variables between the Mechanical and Magnetic Meshes

The iterative coupling technique between the mechanical and magnetic meshes requires the transformation of mechanical quantities (mechanical displacement, velocity) and magnetic quantities (magnetic force) between the grids. In Fig. 7, a possible structure of a grid-hierarchy for an magneto-mechanical system is shown. The problem is first

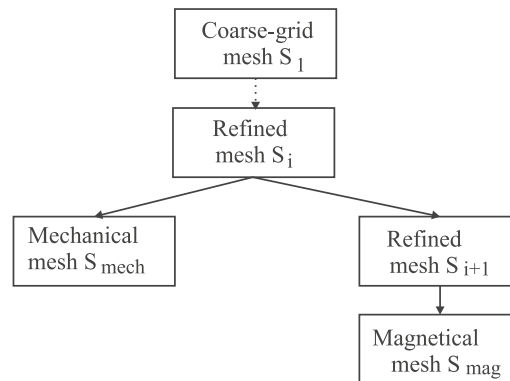


Figure 7: Possible grid-hierarchy of a coupled magneto-mechanical problem.

discretized with a very coarse mesh \mathcal{M}_1 . This mesh is then refined in several steps to a grid \mathcal{M}_i . The grid \mathcal{M}_i is the basis for the mechanical and magnetic mesh which are obtained by adaptive refinement of \mathcal{M}_i . Thereby, the grids for the mechanical and magnetic problems can be adapted to the special properties of the fields. For instance the magnetic mesh can be very fine in eddy-current regions whereas the mechanical mesh remains coarse there. The transformation of the mechanical and magnetic quantities between the different grids is now realized by multigrid transfer operators. These operators are described for instance in [12], [17] and [33].

5 Application Examples

It is not possible to verify the presented simulation technique for coupled magneto-mechanical problems by a mathematical proof. Therefore, the technique was tested and verified by modeling and measuring of two challenging magneto-mechanical devices. The dynamical behavior of the two models (a solenoid valve and an electro-magnetic-acoustic-transducer) was measured and compared to the simulated results. Additionally, the properties of the presented simulation technique with respect to the simulation time were analyzed.

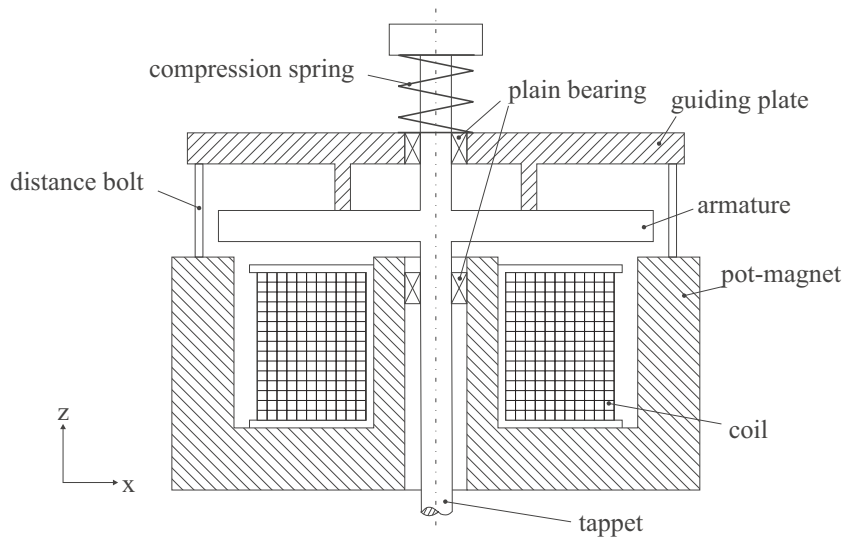


Figure 8: Cross section of the solenoid valve.

5.1 Solenoid Valve

Electro-magnetic actuators are widely used for industrial purposes. Examples are the application in clutches, brakes, relays, loudspeakers, printers and as solenoid valves for pneumatic and hydraulic systems. The reasons for the success of these actuators are

- large magnetic forces,
- large and adjustable strokes, and
- a very robust and stable design.

The disadvantages of electro-magnetic actuators are

- the nonlinear behavior of the magnetic materials,
- strong variations of the magnetic force depending on the position of the armature and
- the magnetic force acts only in one direction.

5.1.1 Design of the Solenoid Valve

In Fig. 8, the principal setup of a solenoid valve is illustrated. The main parts are an armature and a pot-magnet which are made of soft-magnetic material. A prestressed pressure-spring holds the armature in its upper position. If the coil is excited by an electric current, a magnetic force between the pot-magnet and the armature is generated which causes a movement of the armature. The valve-tappet transfers the movement to the mechanical acting mechanism. The outer diameter of the structure is 90 mm , the height 145 mm and the diameter of the tappet is 10 mm . The armature and the pot-magnet consist of unalloyed steel. For both, the guiding-plate and the distance-bolt, alloyed nonmagnetic steel is used and the plain-bearings are made of brass [6]. The coil has 200 turns of copper wire with 1 mm diameter. In Fig. 9, the fully assembled solenoid valve is illustrated.



Figure 9: Solenoid valve with slotted pot-magnet and force sensor.

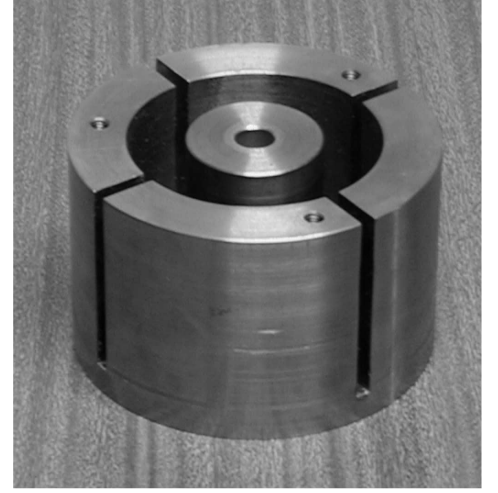


Figure 10: Pot-magnet with four slots which are situated in a relative angle of 90° .

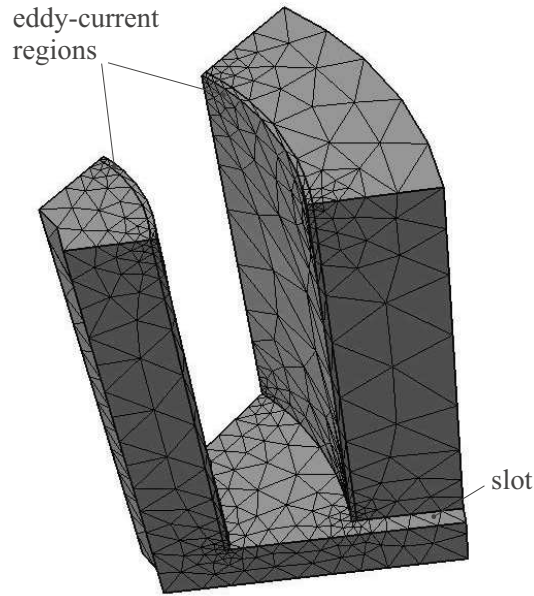


Figure 11: Coarse grid of the pot magnet.

5.1.2 Simulation Model

In Fig. 10, the pot-magnet is displayed. In order to reduce the eddy currents in the material, cuts are milled into the magnet [34]. These cuts destroy the axi-symmetry of the solenoid valve. Therefore, a 3D analysis of the problem must be performed. In Fig. 11, the coarse grid of the pot-magnet is displayed. The radial component of the magnetic induction is zero at the cuts. Therefore, only one eighth of the problem must be considered. At the interface between the pot-magnet and the coil, eddy currents with a very low penetration depth occur. Assuming a maximum relative permeability $\mu_r = 1200$, a specific conductivity $\gamma = 5 \cdot 10^6 \text{ S/m}$ and a maximum frequency of 2000 Hz , we can estimate a penetration depth of (see, e.g., [18])

$$\delta = \frac{1}{\sqrt{\pi \gamma \mu_0 \mu_r f}} = 103 \text{ } \mu\text{m}. \quad (100)$$

The penetration depth was discretized with the help of flat tetrahedron-elements (Fig. 11), where 6 tetrahedron layers for δ were used at the finest discretization level. Therewith, a magnetic edge element discretization with $75 \cdot 10^3$ degrees of freedom was necessary. The mechanical mesh was much coarser and had $20 \cdot 10^3$ mechanical degrees of freedom.

5.1.3 Frequency Response of the Solenoid Valve (Clamped Armature)

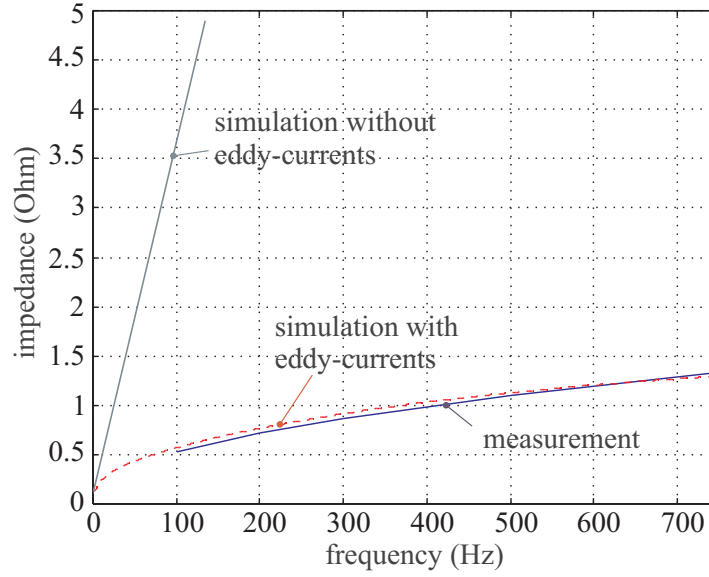


Figure 12: Impedance of the magnetic valve

To guarantee the suitability of the used magnetic FE simulation model, the frequency response of the voltage-current transfer function (impedance) is analyzed. The impedance of the solenoid valve is strongly affected by the eddy currents in the pot-magnet and the armature. Therefore, the determination of the simulated frequency response allows us an evaluation of the used simulation model. Only if the model takes into account the small penetration depths at the surfaces of the magnetic materials, the simulated impedance agrees with the measured impedance.

Let us consider the case of the frequency response for small excitations. With the help of an impedance-analyzer [13], the frequency response of the solenoid valve was measured in the frequency range of 100 to 750 Hz. Since the measurement causes a very small induction in the magnetic circuit, a linear behavior of the magnetic material can be assumed. To determine the frequency response of the valve, a transient simulation is performed. Thereby, the input voltage $u(t)$ is quadratically integrable. Using the Fourier analysis for the input signal $u(t)$ and the calculated current $i(t)$, the frequency response $Z(\omega)$ can be determined by

$$Z(\omega) = \frac{U(\omega)}{I(\omega)}. \quad (101)$$

$U(\omega)$ and $I(\omega)$ denote the input voltage and simulated current which are transferred into the frequency domain. Figure 12 compares the measured and calculated impedance of the solenoid valve. The air gap between armature and pot magnet is zero. Additionally, the simulated impedance for the case of neglected eddy currents is depicted. In this case, the impedance of the valve behaves like the impedance of an ideal inductance which means that it increases linearly as a function of the frequency. The comparison of the curves with and without consideration of the eddy current shows that the eddy currents have a significant influence on the dynamical behavior of the solenoid valve and must definitely be taken into account.

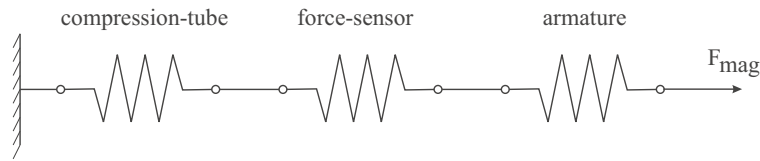


Figure 13: Mechanical equivalent circuit in the case of a clamped armature.

5.1.4 Simulated and Measured Dynamical Magnetic Force (Clamped Armature)

To measure the magnetic force to the armature, the compression spring (Fig. 8) is replaced by a compression tube which suppresses the movement of the armature. Therefore, the vis inertiae can be neglected. Nonlinear vibrations at the contact areas between the guiding plate, the compression tube and the armature are prevented by a prestressing of the mechanical circuit with the force F_v . If the magnetic force F_{mag} becomes larger than the prestressing force F_v , the mechanical circuit is described by an equivalent network which is displayed in Fig. 13. The same force acts at each element of the serial equivalent network, because the vis inertiae is neglected. Therefore, the used force sensor directly measures the magnetic force F_{mag} .

In order to produce a high magnetic force, the coil with 200 turns is loaded by a current pulse. The air gap δ between the armature and the magnetic pot is 2 mm. Since the magnetic circuit is strongly excited by the current pulse, the consideration of the nonlinearity of the used ferromagnetic material is necessary. To measure the magnetization curve, a rod-shaped probe of the used material is measured with the help of a hysteresisgraph (Fig. 14). The used

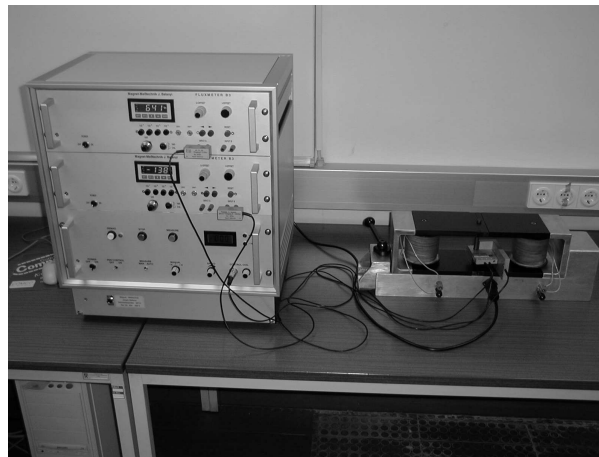


Figure 14: Setup of the hysteresisgraph. Left: Power and measure electronic; right: Double C-yoke with probe [4]

frequency is approximately 0.1 Hz. Because of this low frequency the influence of the eddy currents can be neglected. The magnetic pot, the armature, and the probe were annealed in a nitrogen atmosphere. The annealing process reduces the stresses in the material. The magnetization curve of the used steel St37 is displayed in Fig. 15. The low amount of carbon and other admixtures as well as the annealing process result in a steel with a soft magnetic behavior. Therefore, hysteresis effects can be neglected. In Fig. 16, the simulated and measured magnetic force of the solenoid valve is displayed. The inductance of the valve and the eddy currents in the magnetic circuit delay the rise of the magnetic force. After a time of 4 ms, the maximum of the magnetic force (1200 N) is reached. The maximum of the magnetic induction is 1.9 T. This value of the magnetic induction causes a strong saturation of the material.

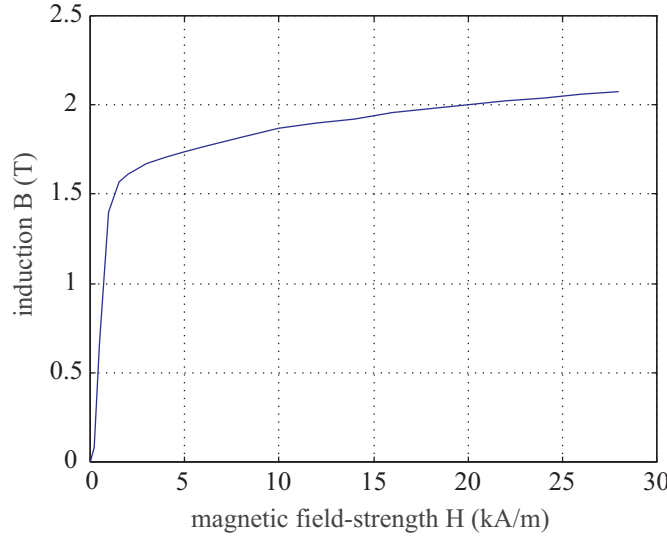
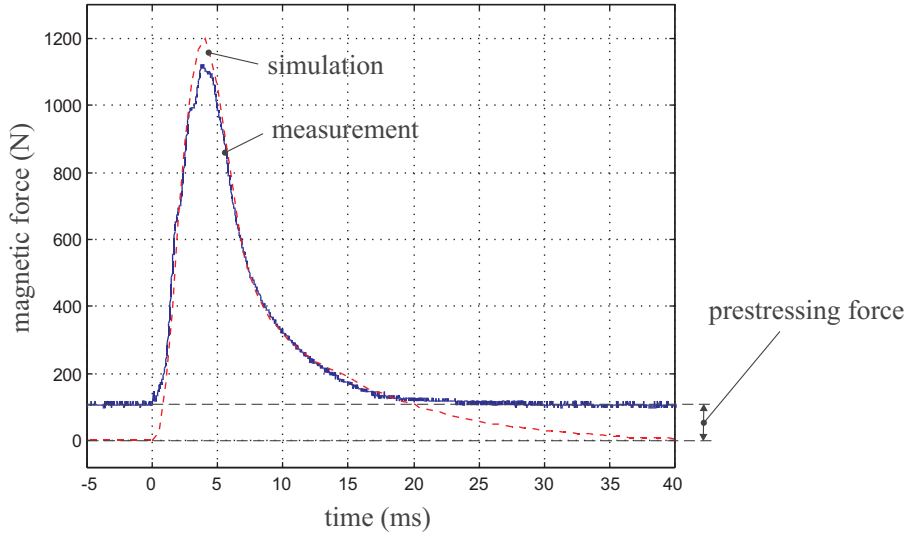


Figure 15: Measured virgin magnetization-curve of the used material St37.

Figure 16: Magnetic force F_z in the air gap (clamped armature).

5.1.5 Simulated and Measured Movement of the Armature

To measure the movement of the armature, the compression spring with a stiffness of $c_{Spring} = 18.3 \text{ kN/m}$ was loaded by a pre-stress force of $F_0 = 198 \text{ N}$. Again, the current in the coil was produced by a capacitor discharge. The transient current was measured with the help of a shunt and the movement of the armature was measured with a Laser-Doppler-Vibrometer [29]. The advantages of the contactless measurement with a vibrometer are the good and linear distance resolution, which is only limited by noise, and a very good dynamic range. In Fig. 18, the simulated and measured movement of the armature are compared. During the first 1.2 ms after switching on the voltage the magnetic force is smaller than the mechanical pre-stress which avoids a movement of the armature. After these first 1.2 ms the magnetic force is large enough to overpower the pre-stress and an acceleration of the armature in the direction of the pot-magnet takes place. Due to the decreasing of the gap between the armature and the pot-magnet the magnetic force is additionally increased. To show the influence of the geometric variations, the magnetic force is simulated with and without considering the geometrical effect of changing the magnetic computational domain (see Fig. 19). At the beginning of the simulation the armature is in rest and the magnetic force is the same for both

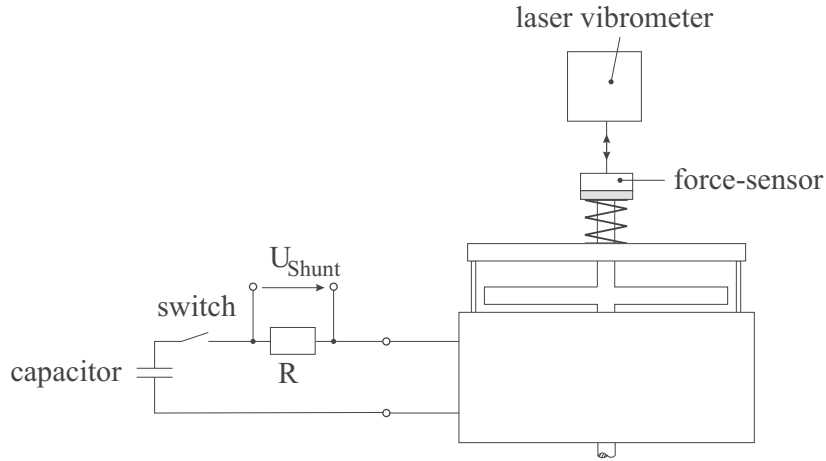


Figure 17: Measurement of the dynamical behavior of the solenoid valve.

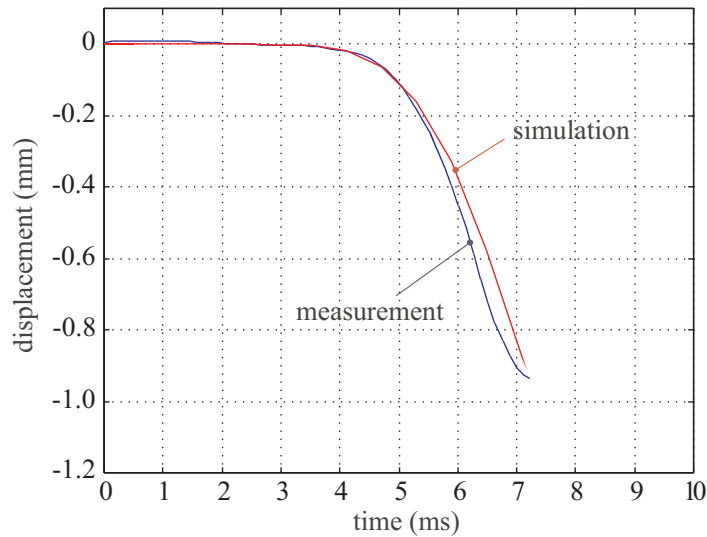


Figure 18: Simulated and measured movement of the armature.

simulations. After approximately 1.5 ms, the air gap is decreased considerably, which causes a stronger raise of the magnetic force in the geometrically nonlinear simulation. Therefore, it is necessary to consider the geometric effect in the simulation of the solenoid valve.

5.1.6 Simulation Times

Figure 18 shows, that the time between switching on the voltage and contact of the armature and pot-magnet is 2.8 ms. The time step width for the simulation is chosen to be $100 \mu\text{s}$ which means that 28 time steps are necessary to simulate the movement of the armature. At each time step one nonlinear magnetic field problem must be solved. For the solution of this nonlinear problem an average of 10 iterations was necessary. Each iteration required the solution of the magnetic FE equation system (80). Therefore, the solution of these systems is the most time consuming part of the simulation process. The considered simulation model with 75000 edge degrees of freedom could be solved with the presented multigrid technique in 21 seconds. The total calculation time for the whole dynamical 3D simulation was 3.05 hours on the SGI Origin with 300 MHz RS12000 processors.

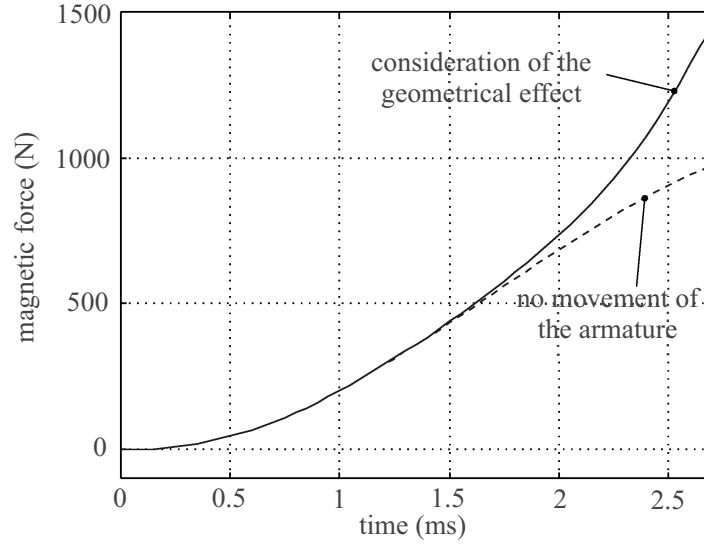


Figure 19: Simulated magnetic force F_z with and without considering the movement of the armature.

5.2 Electro-Magnetic-Acoustic-Transducer (EMAT)

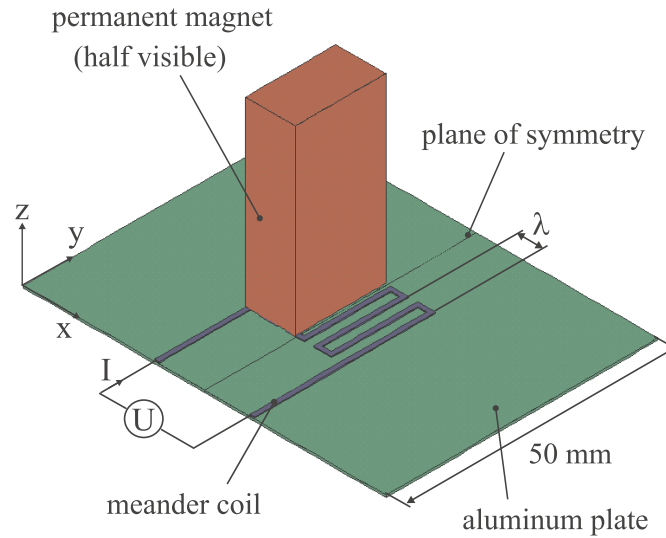


Figure 20: Setup of an EMAT.

Inspecting materials by utilizing ultrasonic waves is a widely used industrial technique [23]. A transducer generates a sound wave which propagates in the material under test. With the help of the position and the shape of reflected and transmitted acoustic waves it is possible to find defects (e.g. cracks) in the material. Piezoelectric transducers are frequently used for the generation and detection of sound waves. For a good transmission of the wave a contact medium must be used between the piezoelectric transducer and the material. Alternative transducer types, which allows a contactless material test, are Electro-Magnetic-Acoustic-Transducers (EMATs) [26]. These are considered in this section.

5.2.1 Generation of acoustic Bulk waves with an EMAT

In Fig. 20, the principal setup of an EMAT is shown. It consists of a permanent magnet (magnetized in z-direction) and a meander coil. The test specimen is situated below the EMAT. The specimen is made of a conductive material.

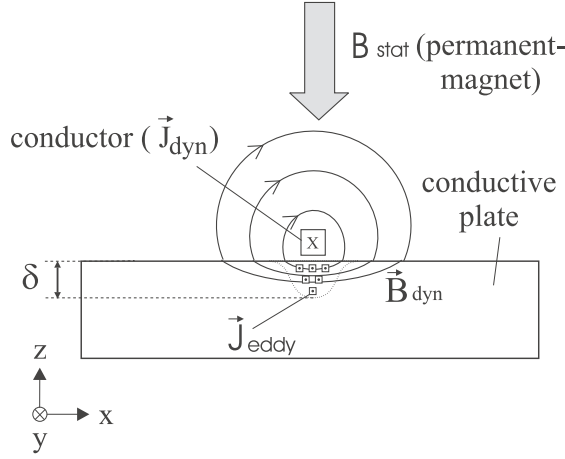


Figure 21: Magnetic field of a conductor near a conductive plate.

If the meander coil is fed by a transient current $I_{dyn}(t)$, a transient magnetic field and eddy currents $\vec{J}_{eddy}(t)$ are induced in the specimen. Due to the Lorentz force

$$\vec{f}_{dyn} = \vec{J}_{eddy} \times (\vec{B}_{dyn} + \vec{B}_{stat}) \quad (102)$$

a mechanical force is generated which leads to the transmission of a sound wave in the specimen. It must be taken into account that the magnetic field \vec{B}_{dyn} and the force density \vec{f}_{dyn} decrease with the distance to the surface of the specimen. The region with an effective generation of a mechanical wave can be determined by the penetration depth (see Fig. 21)

$$\delta = \frac{1}{\sqrt{\pi f \gamma \mu_0 \mu_r}}. \quad (103)$$

In equation (103), f denotes the frequency of the excitation current I_{dyn} , γ the conductivity, μ_0 the permeability in vacuum and μ_r the relative permeability of the used material.

5.2.2 Using EMATs for the Generation of Lamb Waves

Let us assume that the specimen is a thin plate. That means that the thickness d of the plate is small compared to the wavelength λ of the sound wave. If linear elasticity and a plane strain situation is assumed, the existing plate waves can be described by a number of nonlinear equations [22] which can be solved by numerical techniques. The results of this calculation can be demonstrated by a mode dispersion diagram (see Fig. 22). On the abscissa of Fig. 22, the product of excitation frequency and plate thickness, and on the ordinate, the phase velocity are displayed. The abbreviations $S0$, $A0$, $S1$, $A1$, $S2$ and $A2$ refer to the different Lamb modes in the plate. The letter S is used for modes which are symmetrically to the plane of symmetry of the plate, whereas A is used for modes which are antisymmetric to the plane of symmetry. The used number describes the order of the wave in the thickness of the plate. In Fig. 23, the $S0$ and $A0$ modes are displayed.

To excite one of the plate waves with the help of an EMAT, the excitation-frequency must be chosen in such a way that an additive superposition of the conductor forces arise. The maximum excitation can be reached when the wavelength of the chosen mode is equal to two times the distance a between two conductors. Therewith, it is possible to determine the optimal excitation frequency of the different plate modes by drawing the straight line $v = 2a/d$ into the dispersion diagram (see Fig. 22).

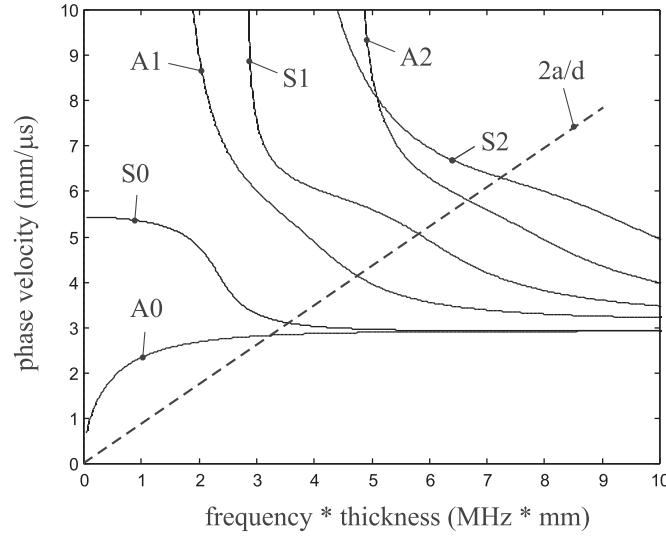


Figure 22: Phase velocity of existing modes in an aluminum-plate.

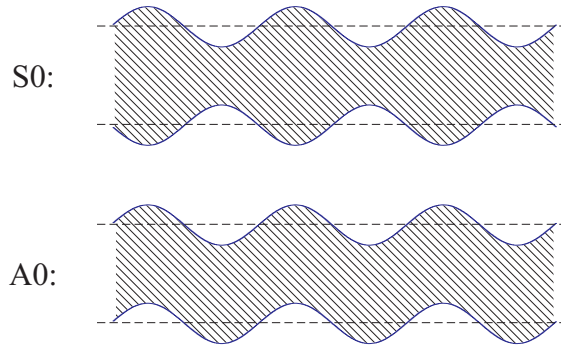


Figure 23: Lamb wave modes in a plate. Above: symmetrical plate wave with zero-order (S0), Bottom: asymmetrical plate wave with zero-order (A0).

5.2.3 Simulation Model

In former publications, for instance, in [26] and [9], a constant magnetic and mechanical field in the y-dimension was assumed. In this case, only a 2D numerical simulation of EMATs was considered. Since the length of the EMATs in y-direction is in the same order of magnitude as the wave-length of the excited plate, diffraction effects occur. These effects are not considered by the 2D models. In this work, a real 3D simulation of the transmission behavior of an EMAT is presented. In Fig. 24, a cross-section of the EMAT and the specimen (aluminum-plate) in the x-z plane is shown. The used material parameters of aluminum are the following [22]:

- Young's modulus $E = 7.0713 \cdot 10^{10} \text{ N/m}^2$,
- Poisson ratio $\nu = 0.3375$,
- specific density $\rho = 2.7 \cdot 10^3 \text{ kg/m}^3$, and
- specific electrical conductivity $\gamma = 35.5 \cdot 10^6 \text{ Sm}$.

The conductors of the meander coil are 1 mm thick and 0.1 mm high. The distance between the permanent magnet and the meander coil is 0.3 mm. The static magnetic field of 0.29 T in z-direction is produced by a Neodym-Iron

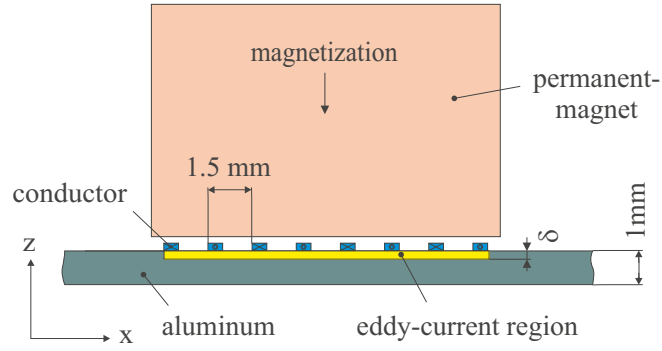


Figure 24: Cross-section of the EMAT and the aluminum-plate in the x-z plane (dimensions in mm).

permanent-magnet. By using the phase velocity diagram (see Fig. 22), the optimal excitation frequency of the A0-mode is $f_{in} = 650 \text{ kHz}$. This frequency results in a penetration depth into the plate which can be approximated by $\delta = 104.7 \mu\text{m}$. This very small penetration depth requires a fine edge element discretization of the aluminum plate

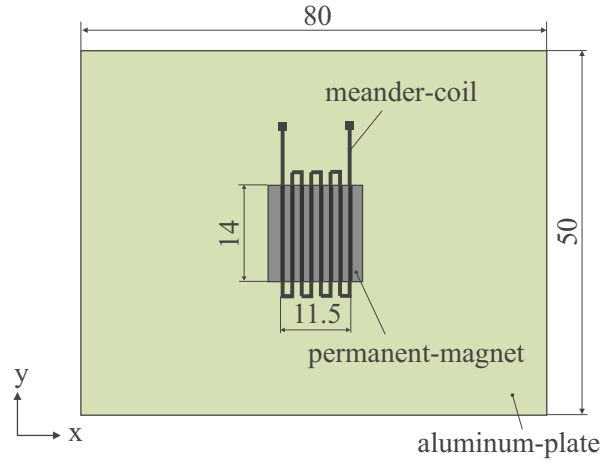


Figure 25: EMAT and aluminum plate in the x-y plane (dimensions in mm).

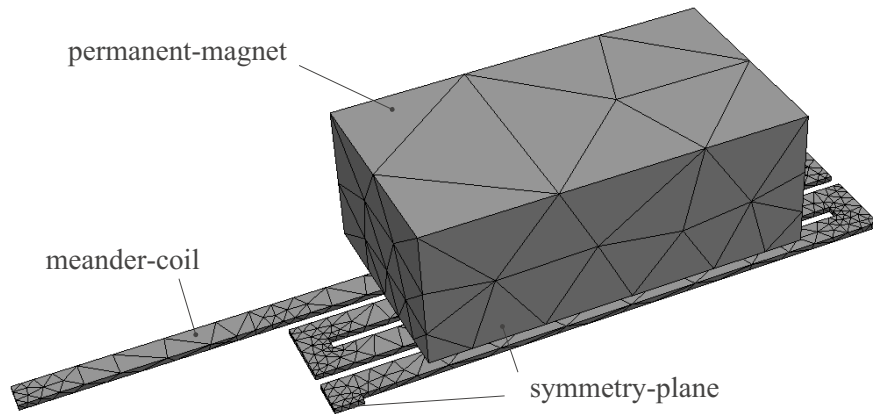


Figure 26: Coarse grid mesh of the meander coil and the permanent magnet.

under the EMAT. In Fig. 26, the coarse grid discretization of the meander coil and the permanent magnet is shown. The model uses the symmetry of the problem in the y-z plane. Since the gradient of the magnetic field in x- and y-direction is weak, flat tetrahedral elements with a length to height ratio of 15 are used. The number of necessary finite elements could be reduced considerably by these flat elements. The height of the coarse-grid elements in the area of the penetration depth is $150\ \mu\text{m}$. To achieve a sufficiently fine resolution of the penetration depth, these elements must be refined twice. This results in elements with a maximal height of $37.5\ \mu\text{m}$. The final magnetic edge element mesh has the following properties:

- 391.500 edge-tetrahedron-elements,
- 342.625 edges (degrees of freedom).

The wave length λ of the excited A0-mode is 3 mm. To describe the propagation of this mode for the maximal side-length e_{max} of the mechanical elements

$$e_{max} = \frac{\lambda}{k} \quad (104)$$

must hold. The so called locking-effect, which results in too stiff elements, is avoided by the use of elements with quadratic basis functions [5]. For quadratic elements, it is sufficient to choose $k = 6$ [21]. With this assumptions the final mechanical FE mesh has the following properties:

- 191.000 quadratic tetrahedron-elements,
- 261.000 nodes,
- 783.000 degrees of freedom.

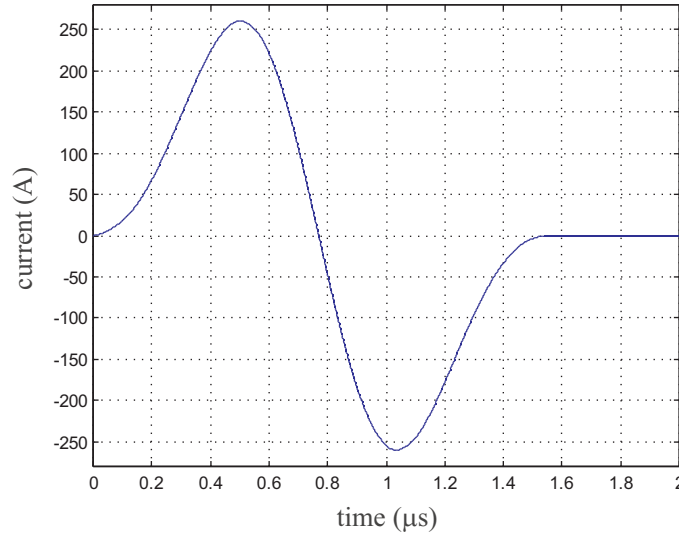


Figure 27: Excitation of a A0 Lamb wave by an current burst.

5.2.4 Simulation of the Generation and the Propagation of a Lamb Wave

By loading the meander coil of the EMAT by a sine current burst, the A0-mode in the plate is excited. The sine burst with a frequency of 650 kHz (see Fig. 27) is filtered by a Kaiser-window which reduces the bandwidth of the burst considerably [25]. The time step of the FE-simulation is chosen with 100 ns. In Fig. 28 and Fig. 29, the simulated transversal components of the generated Lamb wave are shown for different time steps. It can be seen

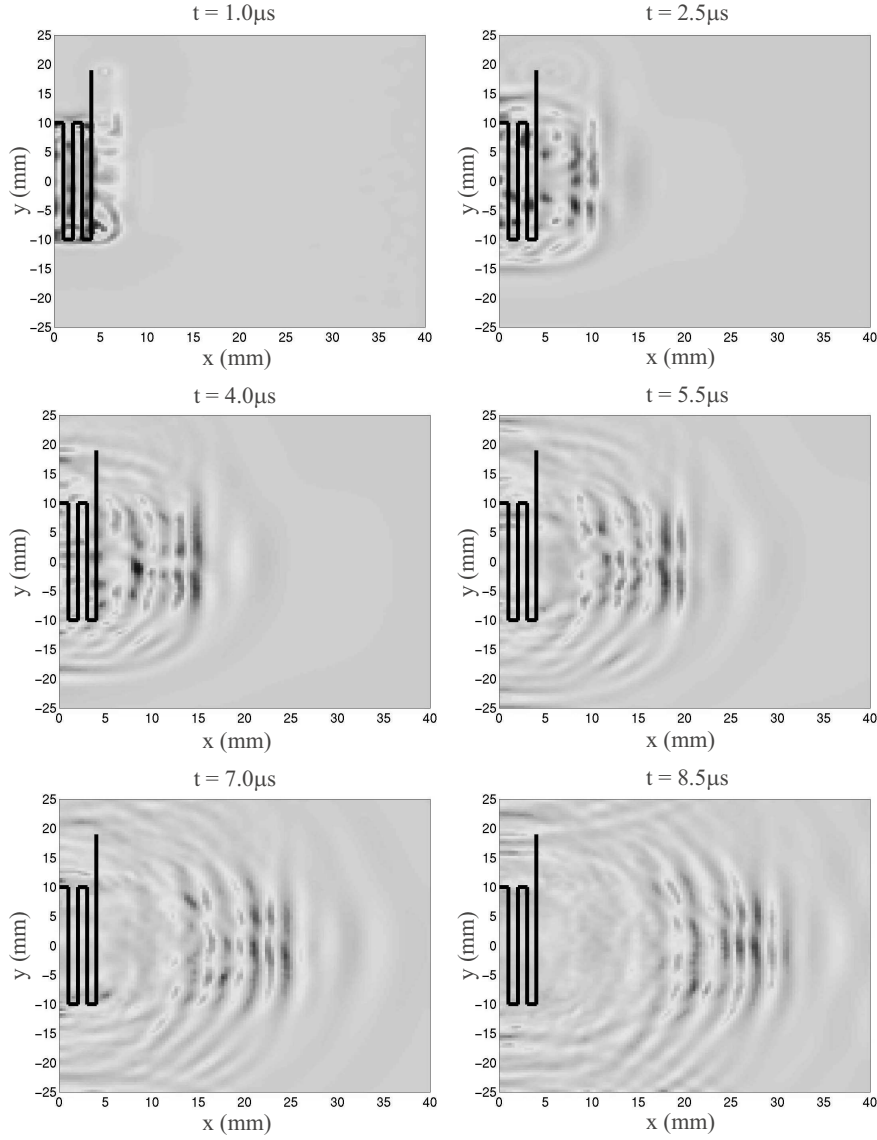


Figure 28: z-component (transversal component) of the Lamb wave at the surface of the aluminum plate.

that the main part of the wave propagates in normal direction to the conductors. Nevertheless, also radiations in other spatial directions occur. After $4 \mu s$ waves in positive and negative y-direction can be detected. These waves are reflected after approximately $6 \mu s$ on the upper and lower boundary of the plate. The shape of the reflected waves can be seen clearly after $8.5 \mu s$. The main wave is reflected on the right plate boundary after approximately $11 \mu s$. The reflected wave can be seen after $15 \mu s$. The shape of the wave for a single point can be seen in Fig. 30. In this case the current excitation burst had 5 sinus-periods. In Fig. 30, the shape of the radiated wave front with its maximum after $11 \mu s$ can be seen clearly. The wave is reflected on the right boundary and reaches the considered point after $21 \mu s$ again.

5.2.5 Measurement and Simulation of the Radiation Pattern of the EMAT

To measure the radiation pattern of the EMAT, the experimental setup which is shown in Fig. 31 is used. To excite the EMAT with sine burst of a frequency of 650 kHz, a RITEC System is used [32]. This system allows the generation of pulses with very high currents. In Fig. 32, the whole measurement setup is displayed. By use of the

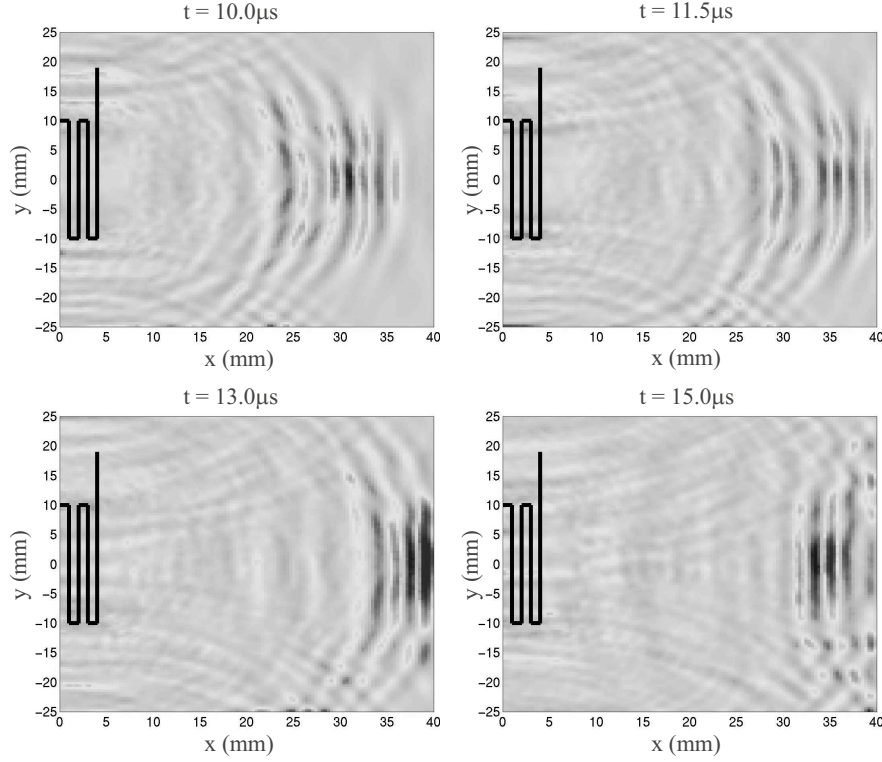


Figure 29: Transversal component of the Lamb wave at the surface of the aluminum plate.

RITEC system a current pulse in the meander coil is generated. The produced mechanical wave is detected with the help of a laser-doppler vibrometer. The output signal of the vibrometer is filtered by the RITEC system and is then displayed on an oscilloscope. By measuring the maximum amplitude of the wave for different angles φ and constant distance r of the vibrometer measurement point, the radiation characteristic can be obtained (see Fig. 33). To avoid big errors of the measurement, the distance r must be out of the nearfield of the EMAT. The size of the nearfield can be estimated by the Fresnel distance [27]

$$r_f = w^2 \frac{k}{10\pi} = 26.6 \text{ mm}, \quad (105)$$

where w denotes the length of the meander coil in y-direction and $k = 2\pi/\lambda$ the wave number. In the simulation, the amplitude of the radiated wave for different angles φ and the distance r was also used to determine the radiation pattern (see Fig. 33).

In Fig. 34, the measured and simulated radiation patterns are displayed. It can be seen that the main radiation direction of the EMAT is in an angle of zero grad (y-direction), but there is also a radiation in other directions. These components can only be calculated by a full 3D simulation of the problem. The reason for the slight distortion of the symmetry of the radiation pattern with respect to the x-axis is the asymmetry of the meander coil.

5.2.6 Computation Times

The dynamical simulation of the Lamb wave in the plate needs an observation time of $15 \mu\text{s}$. 150 time-steps are necessary, because the time-step width of the simulation was chosen to be 100 ns. At each time step, the linear FE equation systems for the magnetic (342.000 degrees of freedom) and the mechanical (783.000 degrees of freedom) problems must be solved. This results in the following calculation times (SGI ORIGIN 300 MHz):

- Magnetic system: 6 MG-CG iterations, 90 s,

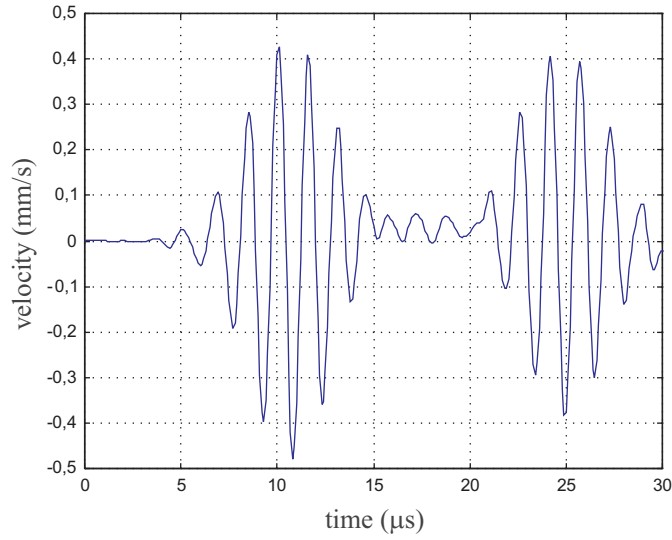


Figure 30: z-component of the surface velocity in a point with the coordinates $x = 20$ mm and $y = 0$ mm.

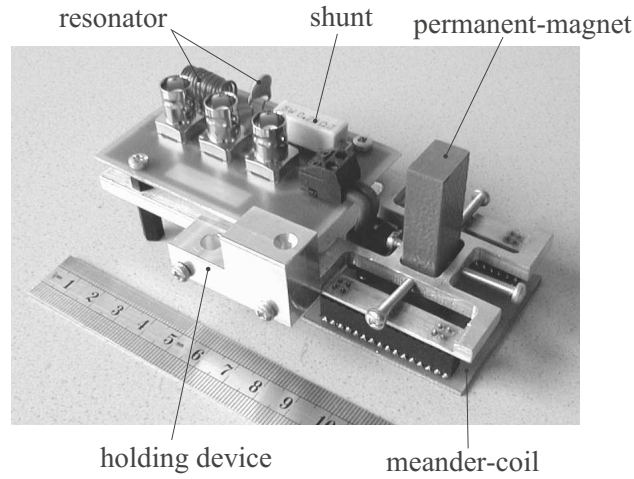


Figure 31: Setup of the EMAT and the integrated amplifier circuit [15].

- Mechanical system: 16 MG-CG iterations, 380 s,
- Calculation of the magnetic induction, projection of the magnetic and mechanical quantities between the both grids, assembling of the right-hand-side etc. : 190 s.

In summary, one time-step needed 660 s. The simulation time for the complete transient analysis was 27.5 hours on the above mentioned computer.

6 Conclusions

In this paper we proposed and tested advanced numerical algorithms for solving transient magneto-mechanical problems. Thereby we used different discretization techniques for the mechanical and magnetic fields. This concerns both the discretization in space and the implicit numerical time integration. In particular, the space discretization can be well adapted to the different behavior of the mechanical and magnetic fields. In order to avoid the solution

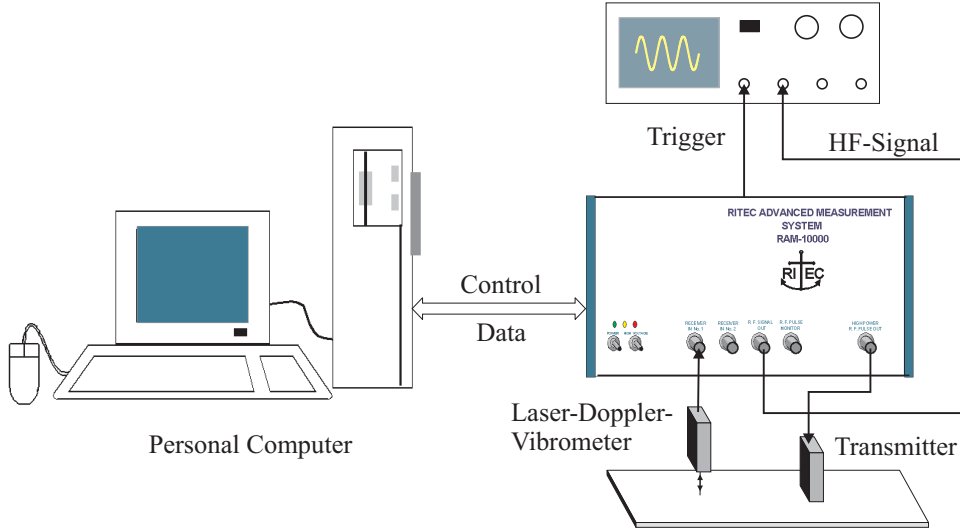


Figure 32: Setup to measure the radiation pattern of a Lamb wave EMAT.

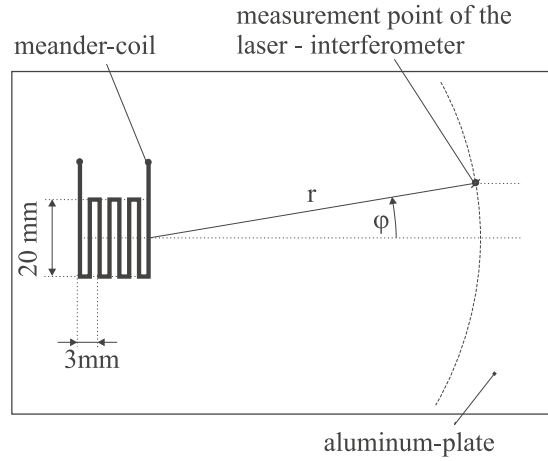


Figure 33: Measurement of the radiation pattern of the EMAT with the help of a laser-doppler vibrometer.

of large systems of coupled mechanical and magnetic finite element equations at each time integration step, we used a coupling iteration procedure that successively requires the solution of mechanical and magnetic systems of finite element equations. The solution of these systems of finite element equations is certainly the most expensive part of the whole numerical algorithms. Whereas no efficient (i.e. linear complexity) solvers are known for the coupled system of mechanical and magnetic finite element equations, such solvers are individually available for the mechanical system as well as for the magnetic system, namely multigrid solvers.

In the second part of the paper we applied our discretization and solution procedure to real-life magneto-mechanical problems and compared the results of our computer simulation with measurements obtained from the real counterpart of our virtual computer model. On the basis of both examples the applicability of the presented simulation-technique to real-life magneto-mechanical problems was demonstrated. The measured and simulated results showed a good agreement. Also the simulation times were comparatively moderate.

Finally, we can summarize that the numerical algorithm proposed in this paper yields a software tool that allows us to simulate quite complex magneto-mechanical sensor and actuator systems in a reasonable time. Therefore, the engineer can use this simulation software very well in the design process. The parallelization of the algorithm, that mainly means the parallelization of the multigrid solvers (see [10, 11, 8]), will considerably accelerate the simulation

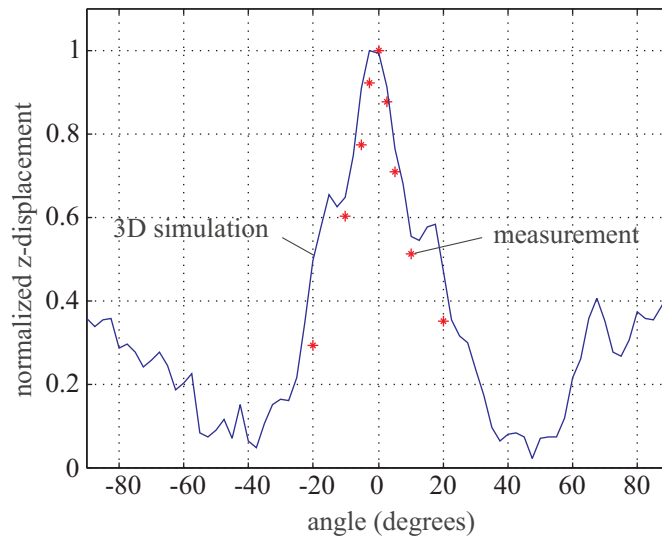


Figure 34: Simulated and measured radiation pattern of a plate-wave EMAT (excitation frequency 0.65 MHz).

on an appropriate parallel computer. Then the simulation can be coupled with an optimization procedure.

Acknowledgements

This work has been supported by the Austrian Science Foundation - ‘Fonds zur Förderung der wissenschaftlichen Forschung (FWF)’ under project F1306 of the SFB F013 ‘Numerical and Symbolic Scientific Computing’.

Addresses: ULRICH LANGER, Institut für Numerische Mathematik, Johannes Kepler Universität Linz, Altenbergerstrasse 69, 4040 Linz, Austria

REINHARD LERCH, Lehrstuhl für Sensorik, Universität Erlangen-Nürnberg, Paul-Gordan-Strasse 3/5, 91052 Erlangen, Germany

MICHAEL SCHINNERL, Spezialforschungsbereich Numerical and Symbolic Scientific Computing, Universität Linz, Altenbergerstrasse 69, 4040 Linz, Austria

JOACHIM SCHÖBERL, Spezialforschungsbereich Numerical and Symbolic Scientific Computing, Johannes Kepler Universität Linz, Altenbergerstrasse 69, 4040 Linz, Austria

MANFRED KALTENBACHER, Lehrstuhl für Sensorik, Universität Erlangen-Nürnberg, Paul-Gordan-Strasse 3/5, 91052 Erlangen, Germany

References

- [1] D.N. Arnold, R.S. Falk, and R. Winther. Multigrid in $H(\text{div})$ and $H(\text{curl})$. *Numer. Math.*, 85:197–218, 2000.
- [2] O. Axelsson. *Iterative Solution Methods*. Cambridge University Press, 2 edition, 1996.
- [3] F. Bachinger, U. Langer, and J. Schöberl. Numerical analysis of nonlinear multiharmonic eddy current problems. *Numerische Mathematik*, 100:593–616, 2005.
- [4] Ballanyi. Handbuch Weicheisenprüfer WP-C. 2000.
- [5] K.J. Bathe. *Finite Element Procedures*. Prentice-Hall, New Jersey, 1996.
- [6] W. Beitz and K.-H. Küttner. *Dubbel, Taschenbuch für den Maschinenbau*. Springer, Berlin, 17 edition, 1990.
- [7] M. Costabel and M. Dauge. Weighted regularization of Maxwell equations in polyhedral domains. *Numer. Math.*, 93(2):239–278, 2002.

- [8] C. Douglas, G. Haase, and U. Langer. *A Tutorial on Elliptic PDE Solvers and Their Parallelization*. SIAM, Philadelphia, 2003.
- [9] K. Ettinger. Numerical Simulation of Electromagnetic Acoustic Transducers (EMATs). Diplomarbeit, Universität Linz, 1998.
- [10] G. Haase, M. Kuhn, and U. Langer. Parallel multigrid 3d Maxwell solvers. *Parallel Computing*, 27(6):761–775, 2001.
- [11] G. Haase and U. Langer. Multigrid methods: From geometrical to algebraic versions. In A. Bourlioux and M.J. Gander, editors, *Modern Methods in Scientific Computing and Applications*, volume 75 of *NATO Science Ser. II, Mathematics, Physics and Chemistry*, pages 103–153. Kluwer Academic Press, Dordrecht, 2002.
- [12] W. Hackbusch. *Multi-Grid Methods and Applications*. Springer, Berlin, 1985.
- [13] Hewlett-Packard. Handbuch Impedance/Gain Phase Analyzer 4194 A.
- [14] R. Hiptmair. Multigrid methods for Maxwell’s equations. *SIAM J. Numer. Anal.*, 36:204–225, 1999.
- [15] M. Hofer. Simulation und Messung der Abstrahleigenschaften von Elektromagnetisch - Akustischen Transducern. Diplomarbeit, Universität Linz, 1999.
- [16] T.J.R. Hughes. *The Finite Element Method*. Prentice-Hall, New Jersey, 1987.
- [17] M. Jung and U. Langer. Applications of multilevel methods to practical problems. *Surv. Math. Ind.*, 1:217–257, 1991.
- [18] E. Kallenbach, R. Eick, and P. Quendt. *Elektromagnete*. Teubner, Stuttgart, 1994.
- [19] M. Kaltenbacher. *Numerical Simulation of Mechatronic Sensors and Actuators*. Springer, Berlin, Heidelberg, New York, 2004.
- [20] M. Kaltenbacher, H. Landes, and R. Lerch. An Efficient Calculation Scheme for the Numerical Simulation of Coupled Magnetomechanical Systems. *IEEE Transactions on Magnetics*, 33(2):1646–1649, 1997.
- [21] M. Kaltenbacher, H. Landes, and R. Lerch. CAPA Verification Manual, Release 3. 1999.
- [22] G.S. Kino. *Acoustic Waves - Devices, Imaging & Analog Signal Processing*. Prentice Hall Inc., 1987.
- [23] J. Krautkrämer and H. Krautkrämer. *Werkstoffprüfung mit Ultraschall*. Springer, Berlin, 5 edition, 1986.
- [24] S. Kurz, J. Fetzer, G. Lehner, and W. Rucker. A novel formulation for 3d eddy current problems with moving bodies using a lagrangian description and bem-fem coupling. *IEEE Transactions on Magnetics*, 34(5):3068–3073, 1998.
- [25] R. Lerch. *Elektrische Messtechnik*. Springer, 2004.
- [26] R. Ludwig and X.-W. Dai. Numerical simulation of electromagnetic acoustic transducer in the time domain. *J.Appl.Phys.*, 69(1):89–98, 1991.
- [27] D.P. Morgan. *SAW Devices and Signal Processing*. Elsevier, Amsterdam, 1991.
- [28] J. Nédélec. Mixed finite elements in R^3 . *Numer.Math.*, pages 315–341, 1980.
- [29] Polytec. Handbuch Polytec Laser Doppler Vibrometer. 1999.
- [30] S. Reitzinger and J. Schöberl. An algebraic multigrid method for finite element discretizations with edge elements. *Numer. Linear Algebra Appl.*, 31(3):223–238, 2002.
- [31] Z. Ren and A. Razek. A Strong Coupled Model for Analysing Dynamic Behaviours of Non-linear Electromagnetic Systems. *IEEE Transactions on Magnetics*, 30(5):3252–3255, 1994.
- [32] RITEC. Operation Manual for Advanced Measurement System Model RAM-0.25-17.5. 1997.

- [33] M. Schinnerl. Numerische Berechnung magneto-mechanischer Systeme mit Mehrgitterverfahren. Dissertation, Universität Erlangen-Nürnberg, 2001.
- [34] K.P. Schmitz. Entwicklung und Untersuchung einer schnellschaltenden elektromagnetischen Stelleinheit. Dissertation, TU Aachen, 1988.
- [35] P.S. Silvester and R.L. Ferrari. *Finite elements for electrical engineers*. Cambridge University Press, 3 edition, 1996.
- [36] J. A. Stratton. *Electromagnetic Theory*. McGraw-Hill, Inc., 1941.
- [37] G. Wunsch and H. Schulz. *Elektromagnetische Felder*. Verlag Technik, Berlin, 2 edition, 1996.
- [38] F. Ziegler. *Mechanics of Solids and Fluids*. Springer, Vienna, 1991.